**University of Twente**
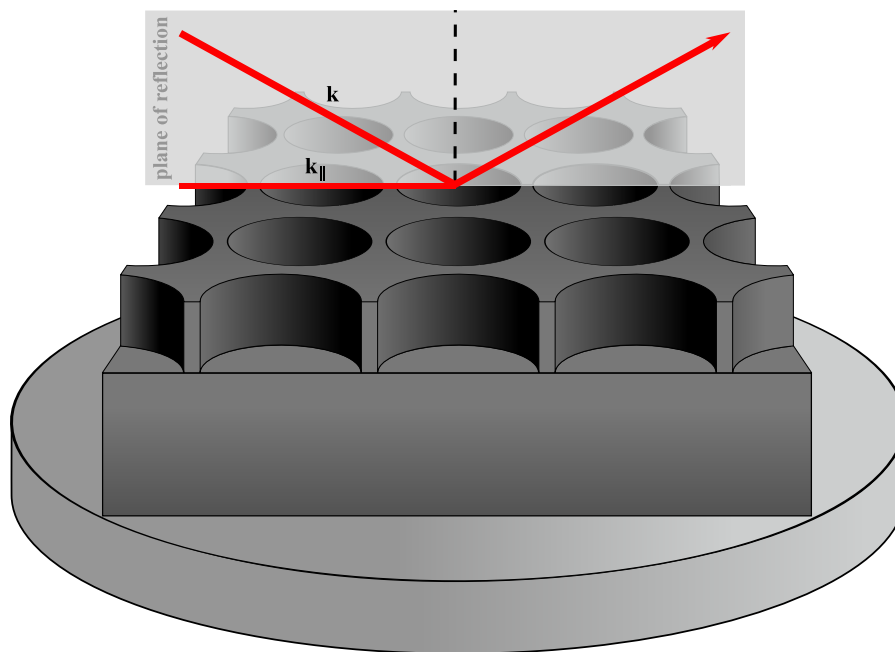**Enschede - The Netherlands**

# Spectral Investigation of a 2-Dimensional Photonic Crystal Slab for mid-Infrared Radiation

R.A.J. Hagen

# Spectral Investigation of a 2-Dimensional Photonic Crystal Slab for mid-Infrared Radiation

University of Twente

Laser Physics and Nonlinear Optics

Faculty of Science and Technology & MESA+ Research Institute

Enschede, September 7, 2007

Graduation Committee:

prof. dr. K.-J. Boller

dr. P. Groß

dr. P.J.M. van der Slot

dr. H.J.W.M. Hoekstra

**Abstract**

This thesis presents spectral investigations of a two-dimensional (2D) photonic crystal (PhC) which has an exceptional large surface ($100mm^2$). The 2D PhC investigated is made from Silicon and was available for fabrication with a novel Laser Interference Lithography (LIL) technique, where the main design purpose was to provide a modified dispersion for photon energies of less than half of the electronic band gap of silicon. Here we present by angular dependent infrared reflectivity and transmission spectra of these crystals as obtained in experiments. Resonance features are observed in polarized reflectivity and transmission spectra in the near and mid-infrared, which arise from coupling of radiation to PhC leaky modes. We determine the quality factor of the experimentally observed features and comparing them with upper limit as calculated for the modes supported by our structure. This comparison provides the first information on the crystal quality obtained by the named LIL fabrication.

# Contents

# Chapter 1

# Introduction

The investigation of third-order nonlinear effects in photonic crystals (PhCs) is of high interest, as these effects might enable an improved temporal and spectral control of propagating light for the purpose of integrated optical devices, such as for optical switching. A switching on the femtosecond time scale can principally be achieved with the real-part (refractive index part) of the third order response, which is called the optical Kerr-effect or the intensity-dependent refractive index. The observation of these effects is hampered by linear absorption and other losses, such as arising from imperfections from the fabrication process. A more fundamental obstacle for fast ($fs$) switching is, however, the imaginary part of the third-order response, called two-photon absorption. When two-photon absorption is allowed, i.e., if the sum-energy of two photons is larger than the electronic bandgap, this would excite population into the conduction band. Once excited, this population would decay rather slowly, with intra-band lifetimes in the $ps$ range, and with up to $ns$ inter-band lifetimes, which would limit the speed of optical switching accordingly. In order to avoid such two-photon absorption we investigate a special PhC with a relatively large spatial period of refractive index modulation. This should shift stop bands into the mid-infrared (MIR), where two-photon absorption is suppressed due to the lack of photon energy. As preparation for later nonlinear studies, the large period enables to characterize the crystal in the near infrared (NIR), at half of the target (MIR) wavelength, where we carried out characterizing reflectivity and transmission measurements. This characterization and a comparison with theoretical models provides valuable information on the linear optical properties of the fabricated crystals which complements a technically more challenging characterization in the MIR.

Several studies on how resonant guiding in 2D photonic crystal appears in reflection [1–7] and transmission [8] spectra were reported before. However, the recent demonstration of a novel type of laser interference lithography (LIL) has made it possible to fabricate large area 2D PhCs also from Silicon and for MIR radiation, while optical studies of the quality of these crystals are lacking so far. In this thesis we demonstrate that resonances

can be observed in reflection and transmission spectra and we determine the quality of the with LIL fabricated MIR PhCs.

In the first chapter we review the theoretical background necessary to understand the experimental results obtained (Chapter 2). In Chapter 3, a brief description of theoretical modeling tools for the calculation of transmission and reflection spectra of the crystal are given. In Chapter 4, the fabrication technique which has been used to make our crystal is explained. Then, the experimental results in transmission (Chapter 5) and in reflection (Chapter 6) are analyzed. Finally, in Chapter 7 conclusions are drawn about the quality of a large area 2D Silicon PhC slab fabricated with LIL.

# Chapter 2

# Theory of Photonic Crystals

*Photonic crystals (PhC)* are composites of materials with different refractive indices, where the materials are arranged in a spatially alternating manner such that the resulting modulation period of the refractive index is in the order of the wavelength [9]. Figure 2.1 shows a schematic illustration. On the left a one-dimensional (1D) PhC is illustrated, which consists of parallel layers of two different materials with indices $n_1$ and $n_2$ and thickness $a/2$. The layers with $n_1$ and $n_2$, are repeated, which results in a superlattice with period $a$. To obtain a two-dimensional (2D) PhC, one could think of the 1D crystal cut perpendicular to the layers with every other slice shifted by $a/2$ as is shown in the middle of Fig. 2.1. Analogously, by slicing the 2D PhC in the horizontal direction, shifting by $a/2$, one obtains a three-dimensional (3D) PhC with a periodicity of refractive material along all directions as illustrated on the right of Fig. 2.1.
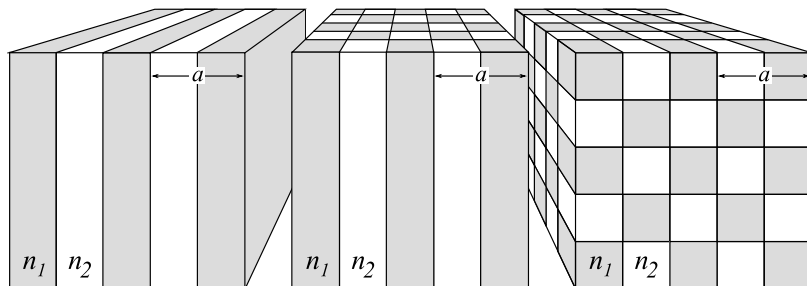


**Figure 2.1:** *Schematic illustration of a 1D-, 2D- and 3D-dimensional photonic crystal.*

With such structure, the propagation of light in PhCs becomes strongly modified, which can qualitatively be understood as follows. For example, a 1D PhC can be seen as Bragg-reflection in a multi-layer mirror. Propagating light is repeatedly redirected by Fresnel-reflection at the material interfaces. Depending on the optical path length difference, which is given by the period $a$ and the refractive index of the layers, the reflections can interfere constructively and destructively, such that light with certain frequencies is forbidden to propagate as in a highly reflective multi-layer mirror.

For 2D and 3D crystals the situation is considerably more complicated because here the redirection of propagating light occurs via diffraction into two and three dimensions, respectively, which also depends on the polarization of the light. Furthermore, the shape of the material boundaries is usually not cubic (as in the right hand side of Fig. 2.1) such that, generally, the theoretical modeling of light propagation in PhCs requires numerical means.

As a basic illustration on how such modeling can be performed we first present in the following a model for the simple case of a 1D PhC. Thereafter, this model is expanded to include the case of a 2D PhC, in order to describe the crystal used in the experiments.

## 2.1  Maxwell Equations

A standard way to describe the propagation of light in photonic crystals is based on the macroscopic Maxwell equations (Eq. 2.1), which were introduced by James Clerk Maxwell in 1864. Here $\mathbf{E}$ and $\mathbf{H}$ are the macroscopic electric and magnetic fields, respectively. $\mathbf{D}$ and $\mathbf{B}$ are the displacement and magnetic induction fields, and $\rho_f$ and $\mathbf{J}_f$ are the free charges and free currents, respectively.

$$\boldsymbol{\nabla} \cdot \mathbf{B} = 0 \qquad \boldsymbol{\nabla} \times \mathbf{E} + \frac{\partial \mathbf{B}}{\partial t} = 0$$

$$\boldsymbol{\nabla} \cdot \mathbf{D} = \rho_f \qquad \boldsymbol{\nabla} \times \mathbf{H} - \frac{\partial \mathbf{D}}{\partial t} = \mathbf{J}_f$$

(2.1)

The type of PhC used in the experiments described in this work does not contain any internal light sources, thus $\rho_f = 0$ and $\mathbf{J}_f = 0$. The Maxwell equations are used to describe the behaviour of electric and magnetic fields in material in general. To simplify the Maxwell equations for the case of photonic crystals four simplifications can be applied.

First, it is assumed that the PhC is subjected only to weak radiation field strengths, such that the induced polarization of the medium remains proportional to the electric field of the light. Second, it is assumed that the dielectric constant $\varepsilon$ at position $\mathbf{r}$ does not depend on the light frequency $\omega$, so $\varepsilon(\mathbf{r}, \omega)$ reduces to $\varepsilon(\mathbf{r})$. The third assumption is that the crystal is macroscopic and isotropic in the sense that, at bulk level, it can be described via an average refractive index, which is only dependent on the direction and polarization, with which the light travels. With these assumptions, one obtains that $\mathbf{D}(\mathbf{r}) = \varepsilon_0 \varepsilon(\mathbf{r}) \mathbf{E}(\mathbf{r})$ and $\mathbf{B}(\mathbf{r}) = \mu_0 \mu(\mathbf{r}) \mathbf{H}(\mathbf{r})$, where $\varepsilon_0 \approx 8.854 \times 10^{-12}$ Farad/m is the vacuum permittivity and $\mu_0 = 4\pi \times 10^{-7}$ Henry/m is the vacuum permeability. Finally, we consider only low-loss (transparent) dielectrics, which means that $\varepsilon(\mathbf{r})$ is purely real.

When taking these simplifications into account, Eqs. 2.1 reduces to a set of equations [9],

$$\boldsymbol{\nabla} \cdot \mathbf{H}(\mathbf{r}, t) = 0 \qquad \boldsymbol{\nabla} \times \mathbf{E}(\mathbf{r}, t) + \mu_0 \frac{\partial \mathbf{H}(\mathbf{r}, t)}{\partial t} = 0$$

$$\boldsymbol{\nabla} \cdot [\varepsilon(\mathbf{r}) \mathbf{E}(\mathbf{r}, t)] = 0 \qquad \boldsymbol{\nabla} \times \mathbf{H}(\mathbf{r}, t) - \varepsilon_0 \varepsilon(\mathbf{r}) \frac{\partial \mathbf{E}(\mathbf{r}, t)}{\partial t} = 0$$

(2.2)

where, in general, $\mathbf{E}$ and $\mathbf{H}$ are still complicated functions of both space and time. However, since the Maxwell equations are linear, the time dependence can be separated out by expanding the field into a set of harmonic modes (Fourier expansion as a function of the light frequency $\omega$). To achieve this, each of these modes $\mathbf{H}(\mathbf{r}, t)$ and $\mathbf{E}(\mathbf{r}, t)$ can be written as a space-dependent amplitude with a harmonic time dependence

$$\mathbf{H}(\mathbf{r}, t) = \mathbf{H}(\mathbf{r}) e^{-i\omega t}$$

$$\mathbf{E}(\mathbf{r}, t) = \mathbf{E}(\mathbf{r}) e^{-i\omega t}.$$

(2.3)

Inserting Eqs. 2.3 into Eqs. 2.2 yields a new set of equations which are no longer a function of time but, instead, scale with the frequency only as an algebraic factor:

$$\boldsymbol{\nabla} \cdot \mathbf{H}(\mathbf{r}) = 0 \qquad \boldsymbol{\nabla} \times \mathbf{E}(\mathbf{r}) - i\omega \mu_0 \mathbf{H}(\mathbf{r}) = 0$$

$$\boldsymbol{\nabla} \cdot [\varepsilon(\mathbf{r}) \mathbf{E}(\mathbf{r})] = 0 \qquad \boldsymbol{\nabla} \times \mathbf{H}(\mathbf{r}) + i\omega \varepsilon_0 \varepsilon(\mathbf{r}) \mathbf{E}(\mathbf{r}) = 0$$

(2.4)

The two divergence equations on the left have the physical interpretation that there are no point sources or sinks of displacement and magnetic fields in the medium. With this, one can eliminate $\mathbf{E}$ from the two curl equations on the right and derive an equation separately for $\mathbf{H}(\mathbf{r})$:

$$\boldsymbol{\nabla} \times \left( \frac{1}{\epsilon(\mathbf{r})} \boldsymbol{\nabla} \times \mathbf{H}(\mathbf{r}) \right) = \left( \frac{\omega}{c} \right)^2 \mathbf{H}(\mathbf{r}) \tag{2.5}$$

This eigenvalue problem is known as the Helmholtz equation. Where $c$ is the speed of light in vacuum. The solutions of the Helmholtz equation for a given crystal, described by $\varepsilon(\mathbf{r})$, are a set of modes for each given frequency [9]. The Helmholtz equation can be solved easily only for homogeneous media, i.e., with $\varepsilon(\mathbf{r}) = \varepsilon(z)$ being constant. The solutions are, e.g., plane wave modes or spherical waves, such as

$$\mathbf{H_k}(\mathbf{r}) = \mathbf{H_0}(\mathbf{r}) e^{-i\mathbf{k} \cdot \mathbf{r}}. \tag{2.6}$$

In Eq. 2.6, the wavevector $\mathbf{k}$ indicates the propagation direction. The dispersion relation of light in a homogeneous medium is a straight line given by

$$\omega = \frac{c}{\sqrt{\varepsilon}} |\mathbf{k}|, \tag{2.7}$$

as can be found by inserting Eq. 2.6 into Eq. 2.5.

In the following two section we are going to develop from a homogenous material to a periodic structure. We will start with the simple case of a 1D structure and continue with a 2D structure.

## 2.2   Dispersion Relation of a 1D PhC

Figure 2.1 showed an example for a 1D photonic crystal (a multi-layer mirror). This structure consists of parallel layers of two different dielectric materials that varies periodically, $\varepsilon(\mathbf{r}) = \varepsilon(\mathbf{r} \pm \mathbf{a})$, i.e., with a superlattice of period $a$. Figure 2.2 displays the solutions of the Helmholtz equation for this mirror. The standard, adopted from solid state physics, is to display the frequency $\omega_n$ as a function of the wavevector $\mathbf{k}$ (in units of $[\frac{2\pi}{a}]$) and a band label number $n$ in order of increasing frequency, while the frequencies is normalized to $[\frac{2\pi c}{a}]$. Figure 2.2 shows that for each $k$-value the spectrum is discrete with $n$ solutions, i.e., there is more than one dispersion curve. Most noticeable is that the frequency of the solutions remains within certain intervals or bands, while there are also frequency intervals or bands for which no $k$-value satisfies the Helmholtz equation (indicated as grey area). This is why Fig. 2.2 is usually called a band diagram. Frequency bands without a solution are called a stopband. Light with frequencies inside a stopband are not allowed to propagate through the PhC (i.e., the mirror is high reflective for these light frequencies). The dispersion curves in Fig. 2.2 has extrema at $m \cdot 0.5$ (where $m$ is an integer) and is periodic with the periodicity $\frac{2\pi}{a}$. The states of light, i.e. the set of eigenvectors $H$ in Eq. 2.5, that belong to a particular frequency, possess periodically occurring $k$-values and are called *Bloch modes*.

As, obviously, the entire information of the dispersion relation is already contained within one period, from $\mathbf{k} = 0$ to $\pi/a$, it is sufficient and standard to display the dispersion of PhCs only in this interval, which is also called the irreducible Brillouin Zone (iBZ). Fig. 2.2 is instructive because similar dispersion curves, with allowed and stopgaps appear also in 2D and 3D crystals, although there the $\mathbf{k}$-vector can assume more than a single direction.

## 2.3   A 2D Photonic Crystal Slab

Figure 2.3(a) shows a schematic illustration of a two-dimensional photonic crystal waveguide similar to the one used in the experiments. The crystal is essentially a high refractive index (Silicon) slab containing periodically air filled holes in a square pattern, which gives high index contrast with regards to the slab material ($n_{Si} - n_{air} = 2.4$). Within the figure two distinct directions in plane with the slab can be recognized, the direction parallel with
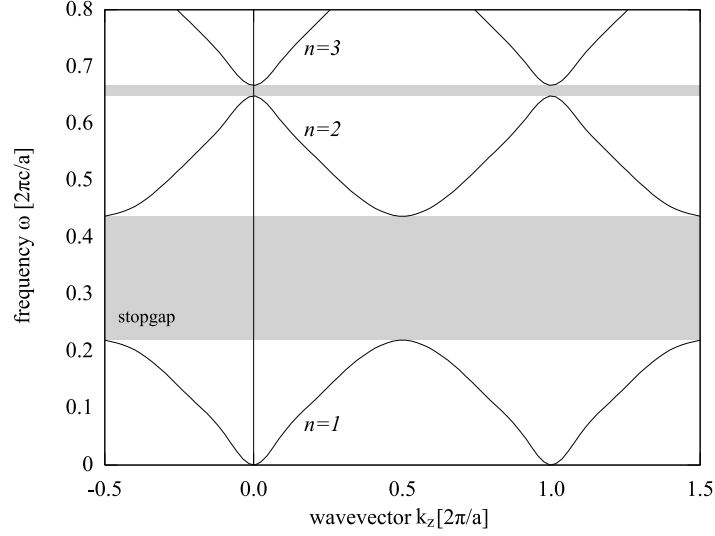
**Figure 2.2:** *Dispersion relation (band diagram) for a 1D PhC. The gray shaded bands indicates stopgaps where no modes are present.*

the x-axis, i.e., along the sides of the square pattern where the index variation period is the smallest. At an angle of 45° with the former directions, i.e., crossing diagonally through the square pattern, the period is largest.

Figure 2.3(b) shows the BZ of the square lattice PhC shown in Fig. 2.3(a). The BZ is a primitive cell of the *reciprocal lattice* (or k-space). The reciprocal lattice is the inverse of the real-space lattice [10]. The points denoted by $\Gamma$, $X$ and $M$ are the high symmetry points, with **k**-vectors $\mathbf{k}_\| = 0$, $\mathbf{k}_\| = \frac{\pi}{a}\widehat{\mathbf{x}}$ and $\mathbf{k}_\| = \frac{\pi}{a}\widehat{\mathbf{x}} + \frac{\pi}{a}\widehat{\mathbf{y}}$, respectively. The high symmetry points enclose the gray shaded triangle called the irreducible Brillouin Zone (iBZ). The high symmetry points are special, because every wave with a **k**-vector extending from $\Gamma$ to the iBZ gives rise to Bragg-reflected waves. For a large PhC, i.e. many holes, a wave undergoes multiple scattering as it propagates through the crystal, but because of the periodicity of the crystal the scattering is coherent. The field can propagate through the crystal in a coherent manner, to produce a standing wave field as a Bloch mode [9,10].
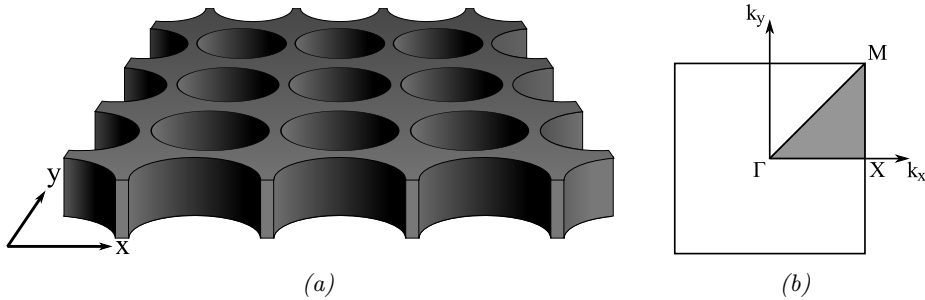


*(a)*                    *(b)*

**Figure 2.3:** *A 2D PhC waveguide slab. (a) Schematic illustration of a 2D PhC slab with a square lattice of air holes introduced into a high refractive slab. (b) Brillouin Zone defined in reciprocal space. The high-symmetry points $\Gamma$, $X$ and $M$ enclose the irreducible Brillouin Zone.*

7

Figure 2.4 shows the band diagram for the PhC of Fig. 2.3. The band diagram is calculated as explained in more detail later (Chapter 3.2). The horizontal axis contains in-plane wavevectors along a path connecting the high symmetry points $\Gamma$–$X$–$M$–$\Gamma$. This is sufficient to show all maxima and minima of all bands [11].
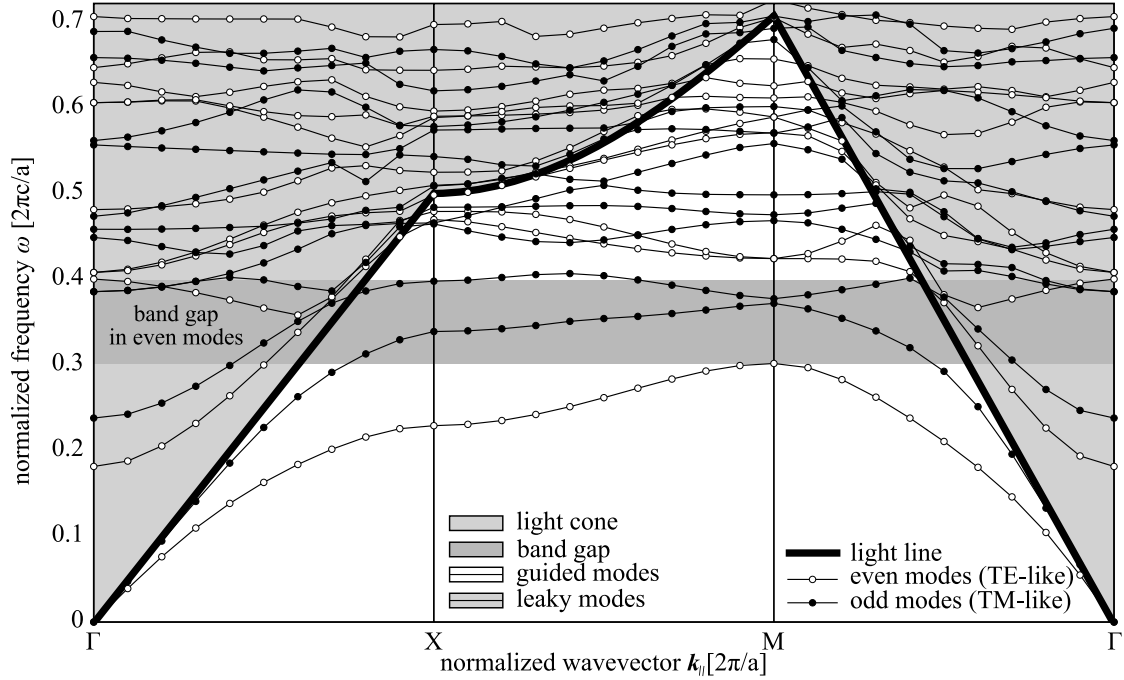


***Figure 2.4:*** *Calculated band diagram of a 2D PhC square lattice slab. The banddiagram is calculated for a Silicon slab with a thickness of 500nm and with hole radius of 0.36μm. The PhC is suspended in air. The open circles indicate the even modes and the filled circles indicate the odd modes.*

In this representation, the thick black line is called the *light line* with $\omega = ck_{||}$, since there is confinement confinement by the slab in the third direction. This light line then represents the frequencies for the $k$-vectors at which modes can leak out of this slab waveguide. The external radiation is a continuum of states outside the waveguide slab and therefore indicated by the gray shaded region, called the *light cone*. Often the light cone is referred to as the *background* or *cladding* [12].

The thin lines with circles show the solutions of the Helmholtz equation, Eq. 2.5. The solutions are calculated for two cases: for light polarized in the plane of the photonic slab and perpendicular to the plane of the photonic slab. The modes of the dispersion relation are presented for the two cases as lines with open circles for the so-called even modes and lines with filled circles for the odd modes. This labelling of the modes as even and odd modes, instead of TE and TM modes, respectively, is based on a mirror symmetry argument, as follows. If one considers the electric field profiles of modes in a thin (smaller then the wavelenght) dielectric slab, then at the symmetry plane ($z = 0$) fields must be purely TE or TM polarized, which is parallel or perpendicular to the $z = 0$

plane, respectively, shown in Figure 2.5. Since the dielectric slab has a certain thickness
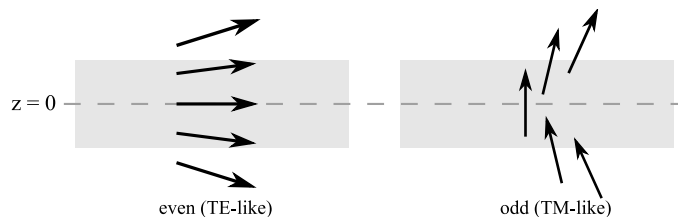


**Figure 2.5:** *Thin dielectric slab with a mirror symmetry at z = 0. The labeling of modes that are mostly parallel, i.e. even, with respect to the mirror plane are TE-like, the modes that are mostly perpendicular, i.e. odd, with respect to the mirror plane are TM-like.*

the fields away of the $z = 0$ plane can no longer be purely TE or TM polarized, because of continuity field should be mostly TE-like or TM-like, which are also called even for polarizations parallel or odd for polarizations perpendicular to $z = 0$, respectively [12, 13].

In-plane with the photonic slab, photonic modes can be completely confined by total internal reflection, when all Bragg-scattering is destructive. Those are referred to as *guided modes*. The guided modes are represented in Fig. 2.4 by the thin lines with open and closed circles that fall entirely under the light line. Theoretically in a perfectly fabricated structure, the guided modes possess an infinite lifetime, which means that there is no energy transfer with external radiation outside the slab. There are also the radiation modes or *leaky modes* which posses a finite lifetime, since they loose there energy to the background with which they overlap and thus can couple. The leaky modes are represented by the thin lines with open and closed circles that overlap with the light cone.

In Figure 2.4 it can further be seen that there is a band gap in the even modes in the normalized frequency range 0.30–0.39, i.e., there is no allowed frequency for any direction or value of the in-plane **k**-vector. In this range of frequencies no guided even modes exist under the light line. As a consequence even-polarized light cannot propagate here in plane with the slab.

## 2.4   Influences on the Dispersion Curves

To get a desired band gap or dispersion curves (here in the mid-IR), there are several parameters that must be chosen properly. This chapter discusses those parameters to give a hint on what there influences are on the dispersion curves or the existence on position or size of the band gap.

*Effects of the slab thickness*

The slab thickness plays an important role in determining whether a photonic crystal slab has a band gap in its guided modes. Johnson et al. [12] have predicted that the optimal thickness will be on the order of half the two-dimensional gap-bottom wavelength. Thicker

slabs would easily support higher-order modes. These higher-order modes lie slightly above the lowest-order mode, preventing any band gap. On the other hand, a slab that is less than half this wavelength only provides a weak perturbation on the background dielectric constant. Although modes will exist, they will lie close to the edge of the light cone and be only weakly guided and any gap will be small.

*Refractive index contrast*

The use of a high refractive index slab is twofold [14]. First, a high refractive index contrast between slab and cladding provides strong field confinement along the vertical direction (i.e. the extent of the guided modes outside the slab is small) allowing a large fraction of each mode to interact with the photonic crystal. In Figure 2.6(a) it is illustrated how the refractive index contrast between the PhC slab and its cladding influences the field confinement. Second, a high refractive index contrast is required between the dielectric material and the holes to open a band gap in the horizontal plane. In practice a contrast of at least 2 is required.

*Slabs with symmetry-breaking backgrounds*

It has been predicted that PhC slabs can be placed on a substrate with only little effect on the band gap as long the substrate is separated from the PhC slab by a sufficiently thick buffer region [12]. This buffer region must have a refractive index low enough, so that a large fraction of the light is still confined in the slab to interact with the photonic crystal slab. This is illustrated in Figure 2.6(b). The wing of the field reaches deeper into the buffer region where the refractive index contrast is low.
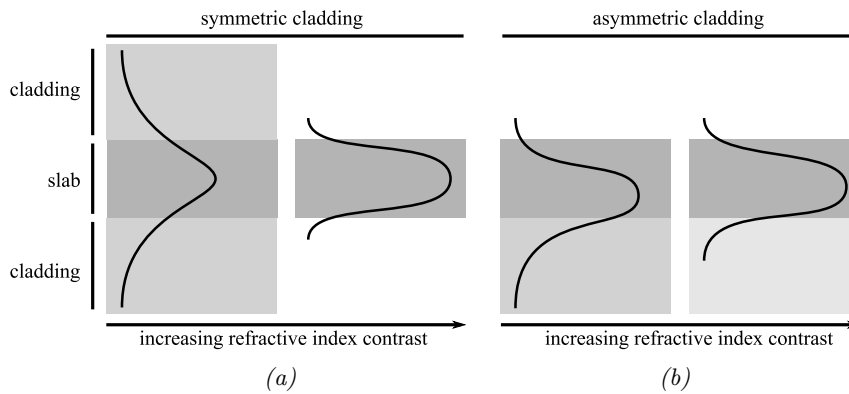


**Figure 2.6:** *Field confinement by cladding material. (a) Field confinement in vertical direction with symmetric cladding. (b) Field confinement in vertical direction with asymmetric cladding.*

*Introduction of periodic array of holes in the slab*

The introduction of a periodic array of holes in the slab has the effect that the dispersion relation is folding into the first Brillouin Zone, and opening a band gap in the guided modes [14]. Another effect of the holes is that it creates an upper frequency cut-off for the guided modes. Figure 2.4 shows that the guided modes are cut-off at a normalized

frequency of 0.7 with the named crystal parameters. Modes above the cut-off frequency Bragg-scatter out of the slab into the background. The cut-off frequency is only determined by the lattice geometry of the array of holes. The PhCs as described in Fig. 2.4 with a square lattice have a cut-off frequency of 0.7, while PhCs with a triangular lattice have their cut-off frequency at 0.66 [14]. The array of holes also has the effect that the guided modes are somewhat shifted to higher frequencies. One reason for this is that the removal of high-index material in the holes lowers the average refractive index of the slab.

## 2.5   Quality Factor & Losses

In Section 2.3 it is mentioned that there is an energy transfer between the leaky modes supported by the photonic crystal slab and the background. This energy transfer only occurs when in-plane wavevectors from the background are equal to that from the leaky modes. Then a fraction of the light couples from the background to the leaky modes and vice versa, energy in a leaky mode gets lost again to the background within a certain decay time or lifetime, $\tau = 1/\gamma$, where $\gamma$ is the decay rate. Thereby the light that leaks out of a mode attains a phase shift relative to the light in the background which gives rise to resonances in reflection or transmission spectra, where the width of these resonances becomes narrower with decreasing decay rate $\gamma$. A widely used measure for the decay rate of the energy stored in damped oscillators and, here, in a certain mode is the quality factor $Q$ of the associated resonance and is defined as

$$Q = \frac{\omega_0}{\gamma},\tag{2.8}$$

where $\omega_0$ is the leaky mode center frequency and $\gamma$ the resonance width at half height. Both $\omega_0$ and $\gamma$ can be obtained from experimental spectra measured in transmission and reflection, as is explained in Section 2.7 [15].

Due to its coupling to the background, the $Q$-factor for a certain leaky mode is principally finite, and given by the design of the PhC. If this is the only mechanism limiting the $Q$-value, namely diffraction produced by the array of holes [16], $Q$ is said to be limited by the so-called *intrinsic losses*. If $Q$ is also limited by other losses, such as fabrication imperfections, this is referred to as *extrinsic losses*.

*Intrinsic losses*

The lifetime given by the intrinsic losses can be seen as related to two roughly independent physical effects to each of which a separate $Q$ value can be addressed, $Q_\perp$ and $Q_\parallel$: Light losses by radiating into the vertical direction, into the background, are addressed by $Q_\perp$ and light that decays into the slab plane is addressed to $Q_\parallel$.

Increasing the mode confinement increases the $Q_\perp$-factor. As modes get more confine-

ment, this eventually dominates over coupling to the leaky modes, resulting in a higher
$Q$-factor. A symmetry-breaking background may cause that the leakage to one side is
more favorable [14].

$Q_\parallel$ is strongly influenced by the radius of the holes. With decreasing hole radius, $Q_\parallel$
increases, since the resonances asymptotically become true guided modes [17].

The physical independence of the described processes associated with $Q_\perp$ and $Q_\parallel$ make
it possible to define a $Q$-factor as given by [18]:

$$\frac{1}{Q} = \frac{1}{Q_\perp} + \frac{1}{Q_\parallel}. \tag{2.9}$$

In the case of a large PhC, i.e., in the limit of many holes, $Q_\parallel$ grows exponential with
the number of cavities formed by a hole in the slab, while $Q_\perp$ remains roughly fixed. By
adding many holes then $Q$ saturates at $Q_\parallel$.

*Extrinsic losses*

Extrinsic losses originate, e.g., from fabrication imperfections and are in general un-
desired. Typically, with current fabrication techniques, the extrinsic losses are one order
of magnitude higher then the intrinsic losses, and thus have an significant influence on
the $Q$-factor [19]. This also explains why it is important to experimentally characterize
the actual $Q$-factor achieved with the particular fabrication method used (here LIL), in-
stead of assuming the theoretically expected $Q$-factor as based only on the crystal's design
parameters.

There are many types of fabrication errors that can contribute to the extrinsic losses:
limited etch depth, roundness of holes, roughness of surfaces or sidewalls [20], tapered
sidewalls [21], hole displacements [22] and irregularities regarding the hole size. How
all these loss factors are reinforcing, or, are counteracting each other is very difficult to
predict. Some of these loss mechanisms have been studied to more detail, but always for
one loss mechanism at a time. In conclusion the extrinsic losses may be better reduced
by trying to improve the fabrication method, assisted by an experimental determination
of the $Q$-values.

## 2.6   Coupling via Vertical Incidence

In order to couple light into the PhC slab, **k**-vectors in-plane with the slab are required.
Obviously, light incident at normal incidence does not contain those **k**-vectors. Neverthe-
less, coupling is possible due to diffraction at the small holes inside the PhC slab. Another
effect expected from vertical incidence to the PhC surface is the occurrence of Fabry-Pérot
interference, due to Fresnel-reflection from the planar transparent layers the PhC consist
of.

*Diffraction of a wave at an aperture*

To illustrate the former diffraction coupling, Figure 2.7 shows a sequence of images for which we calculated the shapes of a plane wave after being transmitted through apertures of different sizes. The resulting pattern behind the aperture can be understood via Huygens's principle as the interference pattern formed by a large number of point sources closely spaced across the width of the aperture. For example, the minima that are visible behind the aperture are the result of destructive interference between the various point sources. In Figure 2.7(a) the aperture has a size that is about five times the wavelength. It can be seen that only at the edge of the aperture the overall wave shows some diffraction while most of the wave is just passing the aperture, maintaining its propagation direction. In Figure 2.7(b) the aperture is comparable to the wavelength, such that diffraction becomes stronger. In Figure 2.7(c) the aperture size is approximately as small as the wavelength. In the case the aperture is so small that it acts like a single point source, thus sending out a hemispherical wave in which the amplitude does not vary much with the emission (diffraction) angle. Correspondingly, a larger fraction light is diffracted close to a right angle and then propagates with a **k**-vector in-plane with the obstructing wall containing the aperture.



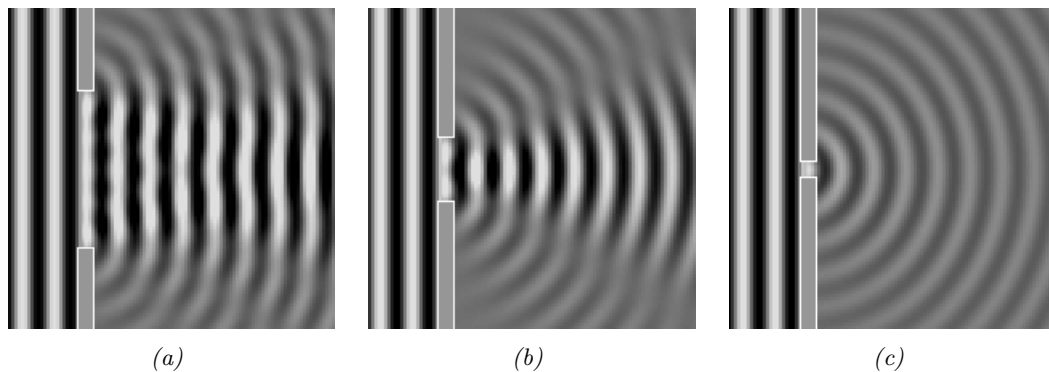<center>(a)           (b)           (c)</center>

**Figure 2.7:** *Diffraction of waves passing different apertures [23]. (a) Aperture size is larger than wavelength. (b) Aperture size is comparable to wavelength. (c) Aperture size is smaller than wavelength.*

*Fabry-Pérot interference by multiple reflections*

To illustrate the origin of Fabry-Pérot fringes, Figure 2.8(a) shows a plane wave (illustrated by rays) that enters a planar transparent layer and undergoes multiple internal Fresnel-reflections between the two reflecting surfaces, before it is (partially) transmitted. Figure 2.8(b) shows the corresponding Fabry-Pérot interference fringes calculated in the transmission as a function of the wavelength $\lambda$ as expressed in Eq. 2.11. The interference is maximally constructive when the optical path length between the transmitted partial waves attain a phase difference $\delta$ that is an integer multiple of the wavelength. From geometrical considerations using Fig. 2.8(a) this phase difference is a function of incident
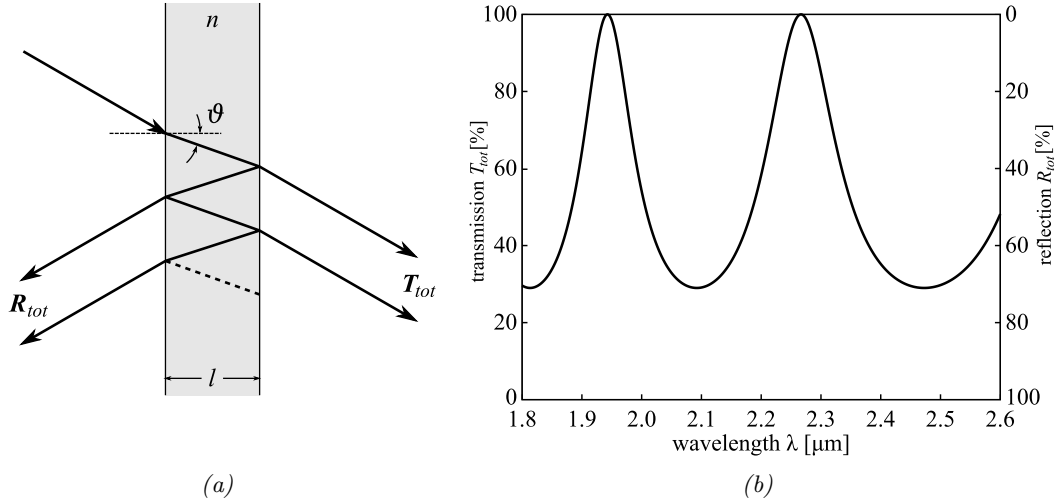
<center>13</center>

**Figure 2.8:** *Fabry-Pérot interference fringes from one layer. (a) Light enters a planar transparent layer that undergoes multiple internal reflections. (b) Fabry-Pérot interference fringes calculated with Eq. 2.11 for incident angle $\vartheta = 0°$, reflection coefficient $r = 0.3$, refractive index $n = 3.4$ and layer thickness $l = 2 \ \mu m$.*

angle $\vartheta$, refractive index $n$ and thickness $l$ of the layer:

$$\delta = \left(\frac{2\pi}{\lambda}\right) 2nl \cos(\vartheta). \tag{2.10}$$

Because, at a single layer, the Fresnel-reflection coefficient $r$ is the same on both surfaces, the transmission $T_{tot}$ can be calculated with Eq. 2.11, which describes the case that absorption and scattering losses can be neglected, i.e., $R_{tot} = 1 - T_{tot}$.

$$T_{tot} = \frac{(1-r)^2}{1 + r^2 - 2r \cos(\delta)}. \tag{2.11}$$

Equation 2.11 shows that the distance between the fringes in Fig. 2.8(b) becomes smaller when the light propagates through effectively more material which creates a longer optical path length difference. This can be realized by increasing the layer thickness, the angle of incident or choosing a material with a higher refractive index. A change to the refractive index, however, also increases the reflection coefficients between the interfaces, which will decrease the spectral bandwidth of the transmission peaks.

We note that Fig. 2.8 describes only the basic principle of how a simple layer structure (here a single layer) creates Fabry-Pérot fringes in transmission. In the PhC's used in our experiments there are actually three layers ($500nm$ Silicon and $3\mu m$ $SiO_2$ on $522\mu m$ Silicon) which is, however, included in the theoretical calculations.

It should be pointed out that layers with $\mu m$-range thicknesses lead to a rather slow variation with wavelength, to broad features that appear like a slow variation of some background spectra. An even thinner layer, say the $500 nm$ top layer of our sample used in the experiments leads to even slower variations of the background.

In contrast to the slow variation of the background spectra, the spectra in reflection and transmission also contains sharp resonances superimposed on the background spectra. These sharp resonances are formed by a second process that takes place, explained in the next section.

## 2.7   Fano Resonances

The sharp resonances which we observed in reflection and transmission spectra on a PhC exhibit all the properties of dispersive line shapes as described by Fano in 1961 [24]. These sharp resonances are of major interest, because it shows how well LIL-fabrication is performed to create photonic slab waveguides.

It shows that the sharp spectral features are actually formed by two independent processes. The first process, direct reflection or transmission modified slowly by Fabry-Pérot interference, is of minor interest. The second process, is excitation of resonances (states, modes) of the photonic crystal, is of major interest, because in this process part of the light is first coupled to the PhC slab and via second diffraction the light leaves the PhC partly in the direction of the directly reflected or transmitted beam and interferes with it. From this resonances appear in the transmission spectrum. It is thus necessary to separate these two transmission processes from each other, i.e., to extract from the spectra the positions and widths of the second (PhC–mode–related) spectral resonances. This can be achieved by Fano-fits to the measured resonances which yield the $\omega_0$ and the width $(\gamma, q)$ independently from the direct reflection or transmission process.

Although the original Fano-function was a description of such asymmetric resonances as based on excitation spectra of inelastic scattering of electrons on Helium atoms, it can also be applied to reflection and transmission spectra on PhC, due to the parallels between the Helium experiment and the experiments in this work. In the Helium experiment electrons either pass the Helium unmodified or excite the Helium atoms to its discreet atomic resonant states. In our experiments the incoming (external) light has the role of the electrons and the discreet atomic resonant states can be seen as the PhC leaky modes.

Fano resonances in the case of photons coupling to the PhC leaky modes is given by:

$$f(\omega) = f_0 \left[ 1 + \frac{q^2 - 1 + 4q(\omega - \omega_0)/\gamma}{1 + 4(\omega - \omega_0)^2/\gamma^2} \right]. \tag{2.12}$$

Here, $f_0$ is the oscillation strength. Figure 2.9 shows how the coupling parameter $q$ determines the shape of the Fano function. A $q$ of 0 means that the energy leaks into a photonic crystal mode without a phase shift, resulting in a symmetric dip in the intensity. For higher $q$ values the resonances become asymmetric and the exact centre frequency $\omega_0$ of $200THz$ is less obvious in the figures.



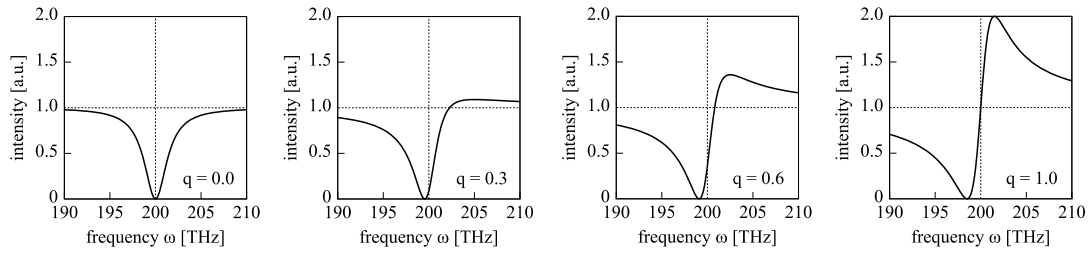**Figure 2.9:** *Fano lineshapes for $\gamma = 0.3THz$, $\omega_o = 200THz$ and different q values. From left to right q value is 0.0, 0.3, 0.6 and 1.0 respectively.*

# Chapter 3

# Computational Modeling Tools

Due to the great complexity encountered with photonic crystals, there are numerous different approaches to predict their properties. Each of these approaches has its own capabilities and limitations. Depending on the goal of the analysis and design of the PhC, the most convenient tool is thus to be selected [18, 19].

Since a full treatment about all available methods goes far beyond the scope of this thesis, we restrict ourself to the three models used in our evaluation of PhCs, namely: The rigorous coupled wave analysis (RCWA), a variation method and a finite difference time-domain (FDTD) method. Each of these methods is implemented as a computer algorithm with its own software known as DiffractMOD, MPB and Meep, respectively. In this chapter we give for each of these software tools a short description, together with its capabilities and its limitations. Something that all of these tools have in common is that they divide space in repeating *computational cells*. Such a computational cell is then filled with a distribution of refractive index materials, to represent one period of the PhC. This data is inserted into equations derived from the Maxwell equations (Eq. 2.1) and evaluated by the simulation tool.

## 3.1   RSoft DiffractMOD

DiffractMOD is a commercially available simulation tool developed by RSoft Design Group, Inc. With DiffractMOD a wide range of scattering situations on structures can be analyzed. It solves full vectorial versions of the Maxwell equations by implementing the rigorous coupled wave analysis (RCWA) method [25]. The software tool calculates reflection and transmission diffraction efficiencies at any diffraction order in the form of a reflection or transmission spectrum.

In the RCWA method a computational cell can have any arbitrary geometry on which the simulation is performed. Within a computational cell a refractive index distribution is

specified that represents the photonic crystal structure. At the surfaces of the computational cell, certain boundary conditions are to be applied, because there is no information from outside the cells available. A common boundary condition is the so-called perfectly matching layer (PML). This represents a (non-physical) material that, in theory, absorbs waves without any reflection, at all frequencies and angles of incidence [26]. Materials and waves adjacent a PML can be interpreted as ongoing at the outside of the computational cell. Surfaces of the computation cell to which no PML is added, are assumed to be repeated by a copy of the computational cell.

Figure 3.1(a) is a graphical presentation of a computational cell filled with an index distribution as given by correspondingly placed materials and on bottom and top end of the cell a PML. There are no PMLs added in the horizontal directions, because the index materials are considered to repeat periodically and infinetely in the horizontal plane. Inside the computational cell of Fig. 3.1(a) the stack of materials represent a photonic crystal slab with an asymmetric cladding (index and thickness of cladding 1 different from cladding 2). The hole being centered in the square xy-plane makes this a square lattice photonic crystal that is periodic with the size of the computational cell.
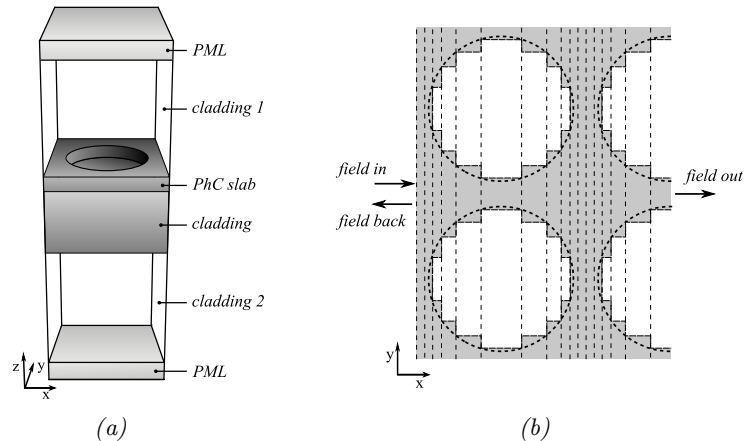


*(a)*                                                    *(b)*

**Figure 3.1:** *(a) Computational cell for a 2D square lattice PhC structure. (b) Fourier expansion of refractive index material in xy-plane.*

The RWCA method expresses the spatial variations of the refractive index as a Fourier expansion of the index as found in slices. Figure 3.1(b) illustrates this for the $xy$-plane. The widths of slices is chosen to model the distribution of the refractive index as closely as practical with a minimum number of slices. The related input and output fields are computed by matching the boundary conditions at every slice. A limitation of this method is that the Fourier expansion introduces a discretization to the distribution of the refractive index, which leads to a staircase effect, as shown in Fig. 3.1(a). The RWCA method in combination with PMLs and the named staircase approximation lead to complex eigenvalue problems. For these reasons RWCA is a method that is sensitive to convergence problems [19, 27].

## 3.2   MIT Photonic-Bands

MIT Photonic-Bands (MPB) is a freely available software package released under the GPL license at Massachusetts Institute of Technology (MIT). MPB directly computes eigenstates and eigenvalues of the Maxwell equations in the frequency domain [28]. MPB implements a variation method, which takes a Fourier transform over an infinite repetition of the computational cell as in Fig. 3.1(a), into all directions to avoid any step discontinuities, except where PMLs are placed.

Figure 3.2 illustrates that the repetition of computational cells introduces a new period in vertical direction. As a consequence, MPB can only calculate the guided modes at high precision, since those are strong localized within the PhC slab. Leaky modes, however, which are not strongly guided, remain therefore primarily dependent on the period introduced in vertical direction. The coupling of leaky modes affecting the guided modes can be reduced to a negligible level by choosing a computational cell that is long in vertical direction, such that the newly introduced periodicity is large. Typically, a few times the lattice constants is sufficient for the height of the computational cell.
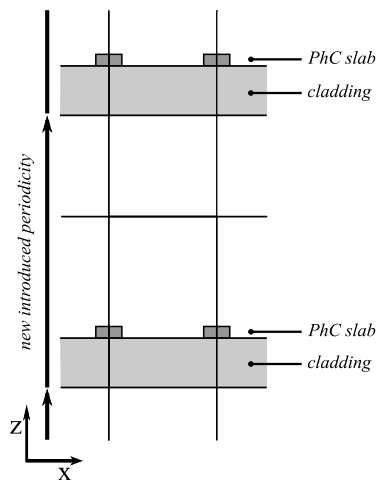


**Figure 3.2:** *Repetition of a computational cell in vertical direction introduces a new periodicity.*

The strength of MPB is that it can calculate band structures and eigenstates very accurately. MPB finds every eigenstate, and even modes with closely spaced frequencies appear as individual modes. The results improves with every new computational iteration. A disadvantage of the frequency-domain methods is that calculations always start at the lowest-frequency eigenstates, up to the desired one [29].

## 3.3   MIT Electromagnetic Equation Propagation

MIT Electromagnetic Equation Propagation (Meep) is a freely available software package released under the GPL license at Massachusetts Institute of Technology (MIT). Meep implements the finite difference time-domain (FDTD) method where the propagation of fields is calculated directly as a function of space and time, according to Maxwell's equations. However, for this it is required to specify, within a computational cell, light sources and flux planes (that model detectors), to generate light and follow its propagation through the structure. The electromagnetic fields are evolved in discreet time steps [18] after the computational cell has been divided in a discreet spatial grid.

Meep can analyze a versatility of electromagnetic situations. The resulting field patterns can be visualized and analyzed in pictures or movies for given light sources. Transmission and reflection spectra can be computed at each frequency separately, or for a broad spectrum via a single computation followed by a Fourier-transformation of as the response to a short pulse emitted by the source. Meep can also calculate the decay time of cavity resonant modes and determine its quality factor $Q$. In contrast with MPB, Meep can have difficulties resolving modes that are closely-spaced in frequencies but Meep calculates all frequency modes at the same time, not consecutively.

# Chapter 4

# LIL-Fabrication of 2D Silicon Photonic Crystals

For the purpose of complete temporal and spectral control of propagating light in the MIR wavelength range, a 2D PhC has been fabricated. Depending on the requirements on PhCs there are several techniques available. A flexible approach to create PhCs with any arbitrary shape is focused ion beam lithography [30] and electron beam lithography [31]. With these techniques holes are written in a sequential manner, which is a strong limitation when large structures are to be fabricated. Other techniques which are less flexible, but provide excellent long-range periodicity are x-ray lithography [32], deep UV lithography [33] and laser interference lithography (LIL) [34]. The latter method is chosen as fabrication method for our sample to produce a PhC with an exceptionally large surface ($100mm^2$), compared to e-beam or ion-beam-fabricated samples that usually are restricted to areas of about $100 \times 100\mu m$. LIL provides an excellent periodicity over a large surface without any stitching errors. The large surface of our sample is a significant advantage for reflection and transmission experiments. The reason is that, particularly in the mid-IR, the light flux even from powerful sources of incandescent light (e.g. lamps) is extremely low after spatial and spectral filtering. With large area PhCs spatial filtering can be much relaxed, which yields a much higher light flux though the sample. In summary, the large area of our LIL-fabricated crystals enables a simple setup and short measurement times, which both contribute to a high signal-to-noise ratio.

This chapter describes the design of our PhC and gives a brief overview on the LIL fabrication method used. A detailed description of the fabrication of our sample is presented in [35]. This chapter finishes with a description of our sample as it is used in the experiments presented in this work.

## 4.1   Design of the 2D PhC

Figure 4.1 displays a schematic illustration of the intended design for the PhC. As a basis for the PhC a Silicon–on–insulator (SOI) wafer [36] is chosen. Silicon is chosen because of its transparency for infra-red radiation, its high refractive index and because it is well known in material science. The wafer consists of three layers: a mono crystalline Si top layer, with a thickness of $0.5\mu m$ and a refractive index of $n \approx 3.4$. The top layer is going to host the holes and serves as the PhC slab. Underneath the top layer is a $3\mu m$ thick $SiO_2$ buffer layer with a low refractive index of $n \approx 1.4$. The bottom layer is a $522\mu m$ thick Si substrate with a refractive index of $n \approx 3.4$ to mechanically support the PhC slab with its buffer layer. The holes in the top layer are intended to obtain a radius of
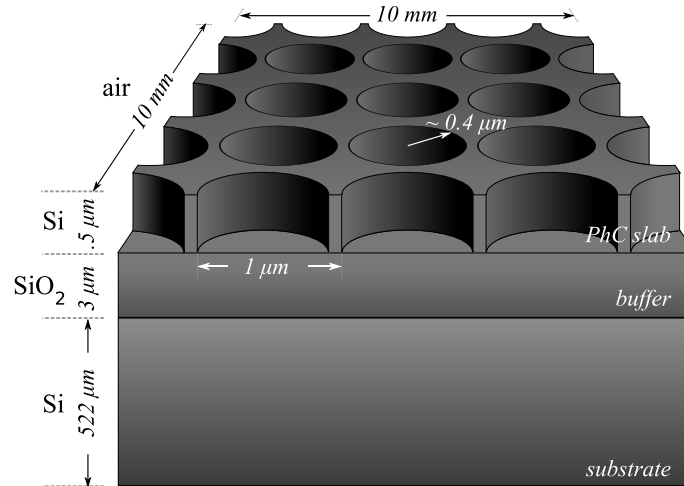


**Figure 4.1:** *Schematic illustration of the 2D PhC as designed for the experiments presented in this work.*

$0.4\mu m$ with square patterned periodicity of $1\mu m$. This design has an expected band gap around a normalized frequency of 0.4 ($\lambda \approx 2.5\mu m$) for TE polarized radiation. Note that, at this wavelength, the photon energy is less than half of the electronic band gap of Silicon which would, in later experiments, allow to study Kerr-induced switching effects without the slowing effect of two-photon absorption.

## 4.2   Fabrication of the 2D PhC with LIL

In order to start with the LIL process the surface of the SOI wafer is first coated with a negative photoresist that responds to UV light, which later is going to serve as a mask with holes through which various etching processes are performed to transfer the pattern into the top layer of the wafer.

For the LIL exposure two continuous-wave UV laser beams with a large ($3cm^2$) cross-section are superimposed to form a well controlled optical interference grating on the

surface of the photoresist. With a first exposure (held under the response threshold of the resist) a $1\mu m$ periodic striped pattern is irradiating the photoresist. A second exposure is followed with the same interference pattern however, with the wafer rotated by $90°$ around its surface normal. As a result of the two exposures, which together surpass the threshold of the resist, a square pattern is written into the photoresist. Heating the wafer to a temperature of $125°C$ for $120s$ leads to the development of the photoresist. The other areas are removed by chemicals, resulting in a mask of photoresist on the top layer. Various etching processes are followed afterwards to transfer the pattern into the Si top layer.

The resulting PhC is displayed in the SEM micrograph of Figure 4.2. The micrograph shows the edge of the PhC to enable a view also inside some of the holes. The micrograph shows that the depth of the holes is seen to be equal to the thickness of the Si top layer, which means that the etching process is stopped, before it would have go into the $SiO_2$ buffer layer. A closer look depicted in the upper right corner of the SEM micrograph shows a sub-micron structure inside the holes and on the walls due to fabrication imperfections. These sub-micron structures causes light to scatter out the PhC during experiments, which attribute to the PhC extrinsic losses (see Section 2.5). And so will do any other unwanted irregularities from the fabrication process like, for instance, dust and cracks.
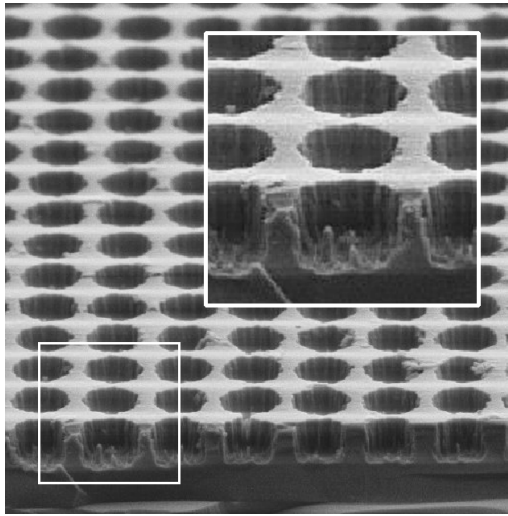


**Figure 4.2:** *SEM micrograph of the with LIL fabricated PhC. The magnified image in the upper right corner shows a sub-micron structure that originate from fabrication imperfections.*

The described fabrication delivered a 2D PhC with a large surface of $100mm^2$. Determined from SEM images the holes have approximately the intended radius of $0.4\mu m$. The measured polydispersity is less than $6\%$ placed in a $1\mu m$ periodic square pattern. Considering that the crystal is immured in air with a refractive index of $n = 1$ the refractive index contrast is $n = 2.4$. The buffer layer and substrate remain unchanged. Table 4.1 summarizes the PhC structure parameters.

***Table 4.1:*** *PhC Structure Parameters*

| | |
|---|---|
| PhC surface dimension | $10 \times 10mm$ |
| hole radius | $0.4\mu m$ |
| lattice periodicity | $1.\mu m$ |
| PhC slab thickness | $0.5\mu m$ |
| cladding thickness | $3.0\mu m$ |
| substrate thickness | $522.\mu m$ |
| refractive index $n_{Si}$ | 3.4 (PhC slab) |
| refractive index $n_{SiO_2}$ | 1.4 (cladding) |
| refractive index $n_{Si}$ | 3.4 (substrate) |

The described PhC, particular due to its large surface, is very suitable for the experiments described in the next two chapters, where light is to be coupled into the PhC modes via the surface of the PhC slab. In the two following chapters, two spectral experiments are presented. The first is a transmission experiment and the second a reflection experiment.

# Chapter 5

# Transmission Experiment

The transmission experiment that is presented in this chapter has been performed in collaboration with our partners in Germany at the Physikalisch-Technische Bundesanstalt (PTB) in Braunschweig, Department of Spektrometrie und mikrooptische Messtechnik. In this experiment the sample of Chapter 4 is placed in a Cary 5E spectrometer to measure its transmittance.

In this experiment the transmission spectrum is recorded as a function of wavelength. The experiment relies on the coupling of external radiation to leaky modes of the photonic crystal, as has successfully been applied earlier by K.B. Crozier, et al. in 2006 [8], however, with free-standing membranes fabricated with much smaller area ($100 \times 100 \mu m$) with an ion-beam technique.

The content of this chapter is organized as follows. First an overview over the experimental set-up in Section 5.1 is given. Then, the transmission spectra are presented in Section 5.2. In Section 5.3 the transmission spectra are compared to calculated transmission spectra to obtain the structural parameters for our PhC as seen by infra-red light. These parameters are used in a second calculation (Section 5.4) to predict the upper limit of the quality factors for the crystal leaky modes.

## 5.1   Set-up for Investigation

The transmission experiment is performed with a Cary 5E spectrometer which is connected to a computer that records the transmittance as a function of wavelength. The spectrum is recorded over the wavelength range of our interest between $1.1 \mu m$ to $2.4 \mu m$. In front of the PhC a linear polarizer is placed to set the polarization.

Since the illumination beam of the spectrometer is diverging a tube is placed in the beam path to obtain a spot-size of $2.5mm$ by $1.5mm$. Note that small area PhC, such as

with an area of $100 \times 100 \mu m$, would have required to reduce the beam area by another factor of 400. Assuming the standard square root law for shot noise this would have increased the measurement time by approximately a factor 20 for the same signal-to-noise ratio. In the far field the beam divergence is $4°$ in vertical direction and $3.4°$ in horizontal direction.

The sample is placed vertical with respect to the direction of beam propagation, in a mount that can rotate the sample around its surface normal. Behind the sample there is a hole in the mount so that the transmitted light can reach a detector placed behind the sample.

## 5.2   Experimental Transmission Results

Figure 5.1 shows the measured transmission spectra as a function of wavelength. The polarization of the light is aligned for three angles with regard to the crystal's symmetry directions, namely along the $\Gamma M$, $\Gamma X$ and an intermediary direction. The transmission is recorded over the wavelength range from $1.1 \mu m$ to $2.4 \mu m$, displayed on the horizontal axis. On the vertical axis the spectral transmittance is displayed.
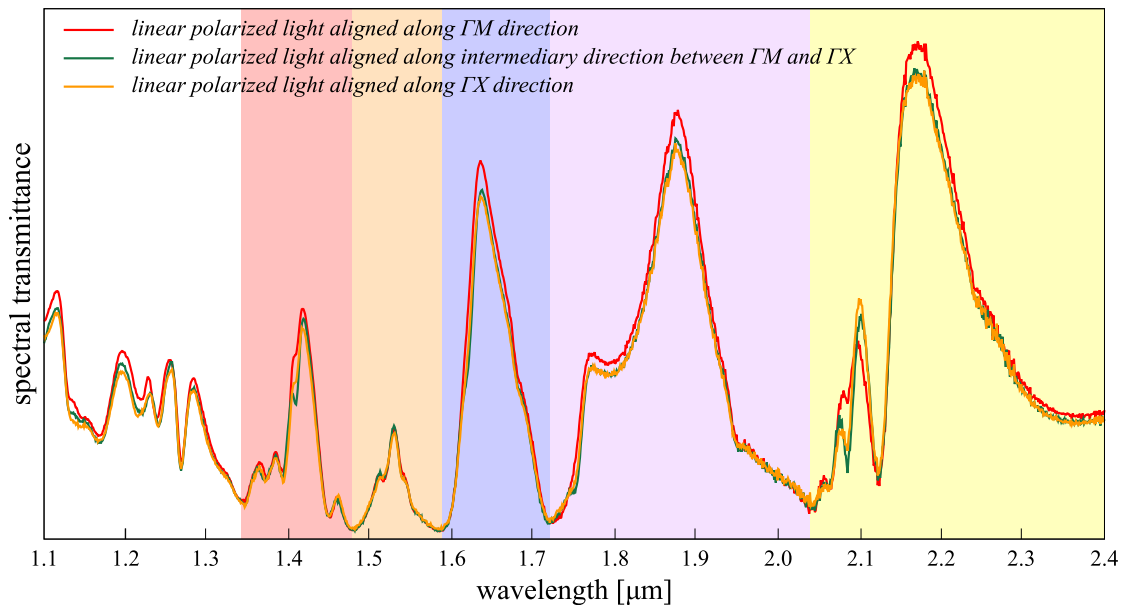


**Figure 5.1:** *Transmission spectra at normal incidence as a function of wavelength. Three measurements where performed with linear polarized light aligned along $\Gamma X$, $\Gamma M$ and the intermediary direction to verify that the spectra are polarization independent.*

Within the transmission spectra there are two types of resonances visible: Fabry-Pérot fringes and sharper resonances superimposed on them. The occurance of these type of resonances have been explained qualitatively in Chapter 2.7.

As a guidance for the eye each Fabry-Pérot fringe is given its own colored background.

The left side of Fig. 5.1 is not given a background color, since we learned from calculations that at these wavelengths there is a high mode density, which excludes to identify single modes within the spectral resolution of the measurements. From this and the small thickness of the top layer resulting in a wide fringes spacing we can not recognize series of Fabry-Pérot fringes in that part of the spectra, as may be suggested by Fig. 2.8.

The high similarity of the three spectra shows that the transmittance is polarization independent at normal incident. Something we find remarkable, since the $\Gamma X$ and $\Gamma M$ direction have different periodicities, $1\mu m$ and $\sqrt{2}\mu m$, respectively. A real physical argument why the spectra must be polarization independent at normal incident, we currently don't have. In Ref. [37] this polarization independence has also been observed in simulations. And has been found to be due to the $90°$ rotational symmetry of the square lattice.

## 5.3 Simulation Transmission Spectrum

In this section the measured transmission spectra of Figure 5.1 are compared to the transmission spectrum calculated with the RCWA model implemented in DiffractMOD (see Section 3.1). In order to get a best fit there are eight structure parameters to vary. Table 5.1 lists these eight parameters as obtained from a best fit. It should be noted that

**Table 5.1:** *DiffractMOD Simulation Structure Parameters*

|  |  |
|---:|:---|
| incident angle | $3.0°$ |
| hole radius | $0.38\mu m$ |
| PhC slab thickness | $0.55\mu m$ |
| cladding thickness | $2.80\mu m$ |
| substrate thickness | $0.01\mu m$ |
| refractive index $n_{Si}$ | 3.45 (PhC slab) |
| refractive index $n_{SiO_2}$ | 1.44 (cladding) |
| refractive index $n_{Si}$ | 3.45 (substrate) |

the simulation has been performed with a substrate thickness of $0.01\mu m$ instead of the actual substrate thickness of $522\mu m$. The reason for this is that the simulations run into a memory error for large computational cells that are required for such thick substrates. With the assumed substrate the reflection coefficient is correct on the cladding–substrate interface and by setting the thickness to well below the wavelength the period of corresponding Fabry-Pérot fringes is strongly increased, far beyond the range accessible in the experiments. This resembles the situation in the experiments where, within the spectral resolution, the fringes from the thick substrate cannot be identified as well and rather form a spectrally independent background as well. It is supposed that the influence of

either a $522\mu m$ or a $0.01\mu m$ thick substrate does not have a significant influence on the resulting spectra.

In Figure 5.2 a measured transmission spectrum (top) is compared to the calculated transmission spectrum (bottom) using the fit parameters of Table 5.1. The figure uses the same variation of background colors as in Fig. 5.1 to highlight the Fabry-Pérot fringes. Most noticeable is the fair agreement between measurement and simulation in width, height and positions of the fringes. With darker colored bands sharp resonances superimposed on the Fabry-Pérot fringes are emphasised that originate from coupling to the PhC leaky modes. Although on comparison between measured and simulated spectra, the sharp resonances do not always exhibit the same shape and position, there is a correspondence of position with respect to their background Fabry-Pérot fringes. Because of this reason we feel confident that the values listed in Table 5.1 are suitable to calculate the expected intrinsic quality factors of leaky modes as described in the next section.
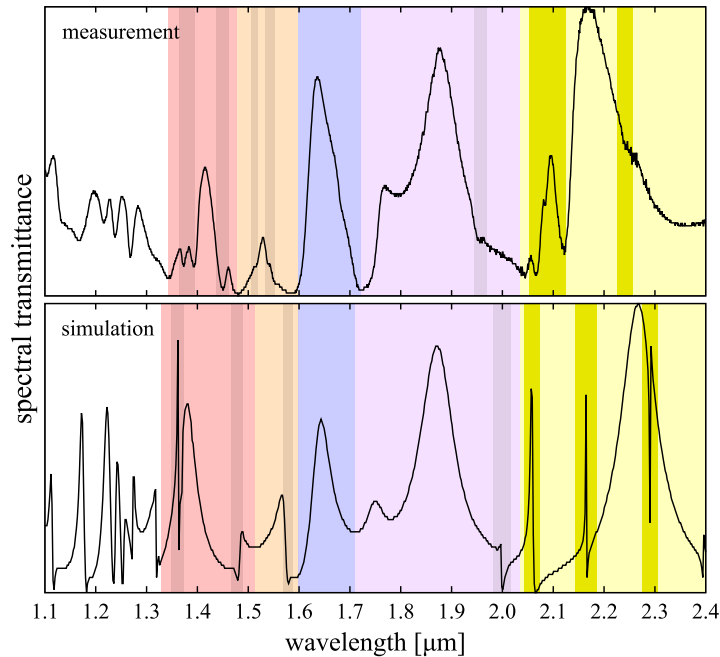


**Figure 5.2:** *Comparison between measured transmission spectrum (top) and simulated transmission spectrum (bottom).*

## 5.4    Calculation of Expected Intrinsic Leaky Modes Q-factors

In order to calculate the intrinsic quality factors for leaky modes with Meep (Section 3.3) a computational cell is specified based on the data in Table 5.1 that where obtained by a fit of the RWCA model to the experimental spectra, except for the substrate thickness. Instead, the Silicon substrate is extended into the lower perfectly matching layer (PML),

such that the substrate is interpreted as extending beyond the outside of the computational cell, i.e. the calculation assumes the substrate to be of infinite thickness.

The strategy to calculate leaky mode quality factors is to place a short pulse light source (containing a broad bandwidth) inside the PhC slab, such that modes with frequencies inside that bandwidth get excited. Once the light source is turned off, light of certain frequencies remains oscillating inside the structure before, eventually, the oscillations are damped out. Meep then Fourier-analyzes this superposition of damped oscillation to extract the PhC mode frequencies and their decay rates or, equivalently, the $Q$-values [18]. In order to obtain the quality factors more accurately, we repeated the calculations for each identified mode frequency, however, with a reduced bandwidth of the light source, centered around each particular mode frequency. The mode frequencies as calculated for TE and TM polarization are listed in Table 5.2 together with their corresponding quality factor. The table show that quality factors have values that vary from 60 to 1800 for TE

***Table 5.2:*** *Meep Q-Factor Calculations*

| TE | | TM | |
|---|---|---|---|
| norm. frequency | $Q$-factor | norm. frequency | $Q$-factor |
| 0.835 | 262.65 | 0.945 | 313.68 |
| 0.820 | 60.07 | 0.927 | 443.72 |
| 0.815 | 1868.60 | 0.896 | 295.51 |
| 0.787 | 841.53 | 0.873 | 255.33 |
| 0.775 | 260.94 | 0.847 | 311.22 |
| 0.750 | 402.72 | 0.828 | 1120.21 |
| 0.744 | 95.27 | 0.815 | 462.96 |
| 0.734 | 134.43 | 0.795 | 606.25 |
| 0.724 | 62.93 | 0.779 | 149.72 |
| 0.715 | 87.20 | 0.759 | 1486.57 |
| 0.708 | 492.88 | 0.739 | 324.18 |
| 0.704 | 189.21 | 0.725 | 95.37 |
| 0.700 | 245.49 | 0.719 | 358.63 |
| 0.651 | 193.77 | 0.704 | 161.14 |
| 0.597 | 68.84 | 0.702 | 139.94 |
| | | 0.658 | 1536.08 |
| | | 0.603 | 273.22 |

modes, and values of 90 to 1500 for TM modes.

The distribution of the quality factors are shown in the histograms of Figure 5.3, where the lhs histogram is for TE polarization and the right histogram is for TM polarization.
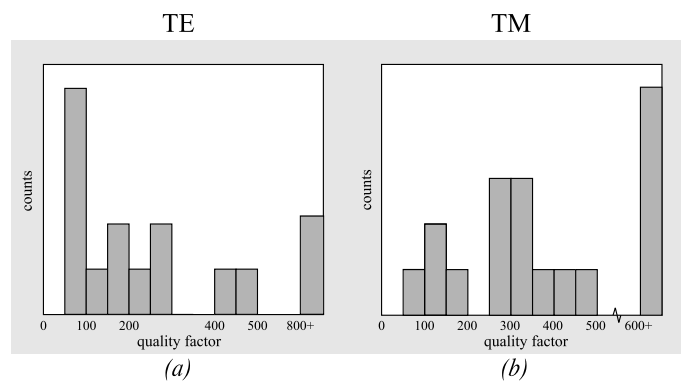
*Figure 5.3:* *Quality factor histograms: (a) TE polarization, (b) TM polarization.*

# Chapter 6

# Reflection Experiment

In this chapter, reflection experiments are described, as performed at the University of Twente, Laser Physics and Nonlinear Optics (LPNO) group using a homebuild set-up. In this experiment the sample as described in Chapter 4 is characterized.

In Section 6.1 we describe the principle of the experiment is explained, followed by an overview of the experimental set-up in Section 6.2. Then, the reflectivity results are presented in Section 6.3. In Section 6.4 the reflectivity results are analyzed and the quality factor for the PhC leaky modes are extracted.

## 6.1   Principle of Investigation

The dispersion of leaky modes of the PhCs can be reconstructed based on resonant coupling observed in reflectivity measurements as a function of wavelength and incidence angle. The technique relies on the coupling of external radiation to leaky modes of the photonic crystal, and has successfully been applied earlier by V.N. Astratov, et al. in 1998 to thin, ion-beam fabricated membranes of much smaller area [1,38]. By recording the reflection spectra for a number of incidence angles along the two symmetry directions $\Gamma X$ and $\Gamma M$, particular resonances shift in wavelength and dispersion curves of the leaky modes can be constructed.

Resonant coupling only occurs when the projected wavevector $\mathbf{k}_\parallel$ of the incoming beam matches the wavevector of the photonic leaky modes. Figure 6.1 displays $\mathbf{k}_\parallel$ as the projection of the incoming wavevector $\mathbf{k}$ along one of the symmetry directions. The symmetry directions $\Gamma X$ and $\Gamma M$ are selected by mounting the sample on a rotation stage that can rotate around the sample surface normal. A second rotation stage (not drawn in Fig. 6.1) is required to vary the incident angle $\vartheta$. The length of $\mathbf{k}_\parallel$ is a function of the
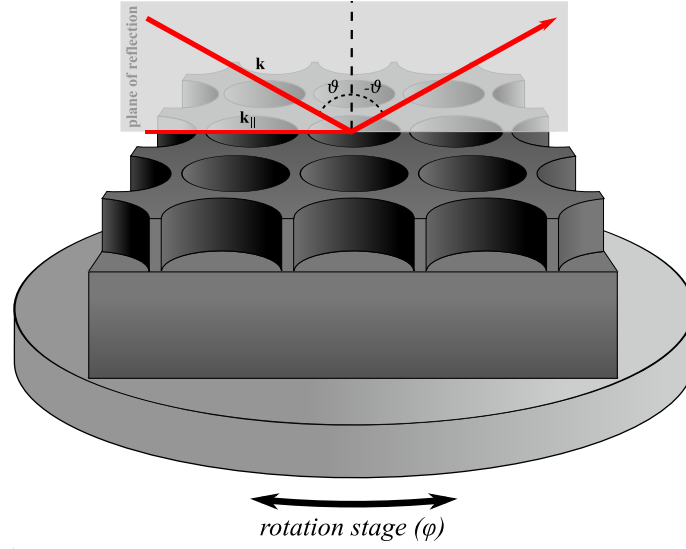
**Figure 6.1:** *Geometry for reflection experiments. A collimated incidence beam is send under an angle $\vartheta$ to the photonic crystal. The reflection is measured under an angle $-\vartheta$. By rotation of the sample, the symmetry directions $\Gamma X$ and $\Gamma M$ are selected.*

incoming wavelength $\lambda_{air}$ in air and the angle of incidence $\vartheta$:

$$\mathbf{k}_{\parallel} = \mathbf{k}\sin\vartheta = \frac{2\pi}{\lambda_{air}}\sin\vartheta. \tag{6.1}$$

Based on the symmetry direction selected, via the relative orientation of the E-field and the crystal rotation, the incident angle $\vartheta$ of the light and the wavelength, corresponds to exactly one position inside the light cone of a banddiagram. So, if the symmetry direction and the incident angle are kept constant during one measurement, changing the wavelength corresponds to a movement along one of the dotted lines drawn inside the banddiagram of Figure 6.2. Each dotted line correspond to an angle $\vartheta$. Fig. 6.2(a,b) gives the $\Gamma X$ and the $\Gamma M$ direction of the banddiagram, respectively. Depending on the alignment of the light polarization perpendicular or parallel to the plane of reflection, only even or odd modes are excited, respectively. For simplicity only the odd modes are displayed in the figure. By scanning the wavelength, one scans the $\mathbf{k}_{\parallel}$-vectors from the background which is in-plane with the PhC slab, as given by Eq. 6.1. Energy transfer to the PhC leaky modes and thus resonances in the reflectivity only occur when the $\mathbf{k}_{\parallel}$-vector equals the PhC leaky mode wavevector. Thus by identifying the frequencies of resonances and their change with the angle of incidence, one can sample the bandstructure of leaky modes.

In order to select any particular position in the light cone one needs a set-up with the possibility to illuminate the sample under known angles $\vartheta$ and $\varphi$ and with a proper beam shaping to provide a sufficient angular resolution. The next section describes our set-up in order to fulfill these criteria.
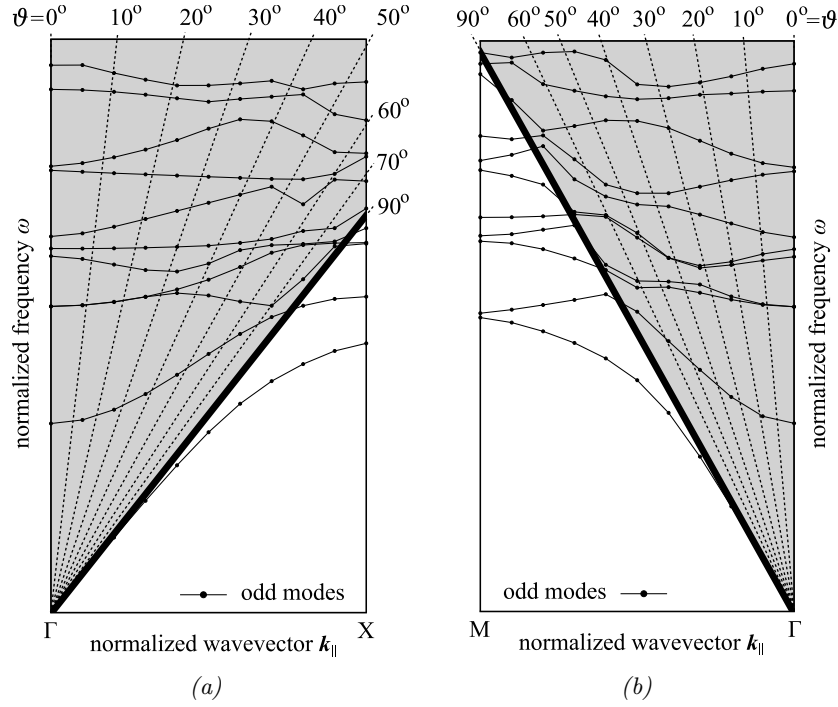
**Figure 6.2:** *ΓX and ΓM direction of a banddiagram. The dotted lines correspond to the angle of incidence ϑ.*

## 6.2  Set-up for Investigation

For the precision required single reflection resonances and their angular dependence it is necessary to optimize both the spectral and spatial resolution of the set-up. A good spatial ($k$-vector) resolution is needed to accurate select a position inside the light cone. The spectral (frequency) resolution will mainly limit the contrast of the resonances in the reflection spectra.

Figure 6.3 displays a schematic illustration of the set-up used. A $250W$ quartz tungsten-halogen (QTH) radiation source (Oriel 66995) driven by a stabilized current supply (Oriel 69931) generates a broad spectrum in the infra-red. The light is focused with a $150mm$ focal
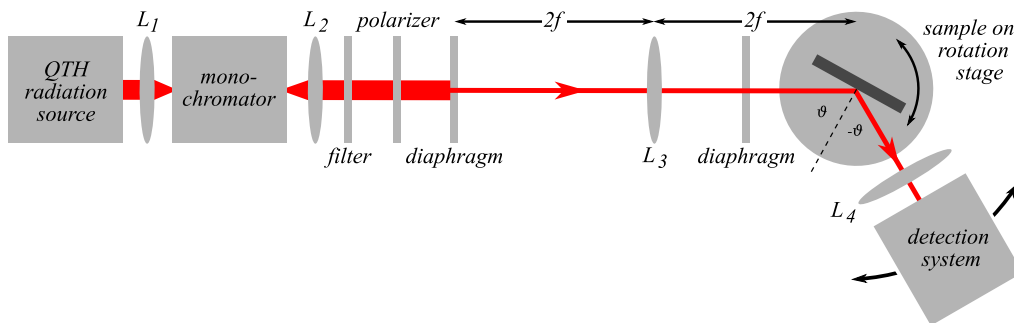


**Figure 6.3:** *Schematic illustration of a home build out of plane reflectivity set-up.*

length plane convex lens ($L_1$) into a monochromator (Hilger and Watts) that selects the desired wavelengths between $1.1\mu m$ to $1.9\mu m$. The lens and the monochromator are set to the same acceptance angle for efficient throughput. The monochromator has a grating of 750 $lines/mm$ and entrance/exit slits widths set to $0.75mm$, which gives a spectral resolution of $3.5nm$. Light leaving the monochromator is focused by a second lens ($L_2$) to an adjustable diaphragm and travels through a high-pass filter which blocks all wavelengths below $1\mu m$ that leave the monochromator via higher order diffraction. With an IR polarizer (Thorlabs LPNIR050) the TE or TM field is set either parallel or perpendicular to the plane of reflection. The following adjustable diaphragm makes part of a diaphragm–lens–diaphragm–sample configuration such that the image of the first diaphragm is relayed onto the sample. The diaphragms limit the beam spotsize to $3mm$ at the center of the sample. The diaphragm–lens–diaphragm–sample configuration yields a full beam divergence of about $\Delta\vartheta = 1°$. The sample is placed in a mount that enables rotation along two axis, such that $\vartheta$ and $\varphi$ can be varied as shown in Figure 6.1. The sample itself is placed at the center of the two required rotation stages such that always the same area of the sample is illuminated. About 30% of the light is reflected at the Si surface of the sample. With lens $L_3$ the reflected light is collected and projected on a lead sulfide (PbS) detector (Newport 70323). Since the set-up is optimized for its resolution, most light is lost along the set-up (monochromator and diaphragms) which makes the detectability of the light more difficult. To improve the signal–to–noise ratio (S/N) the detector is used in combination with an optical chopper and a lock-in amplifier (Princeton Applied Research Corp., model 129A) this way nano Watt power levels could be detected with a typical S/N of better than 10.

## 6.3 Experimental Reflectivity Results

Figure 6.4 shows the measured reflectivity spectra as a function of wavelength for the two symmetry directions $\Gamma X$ and $\Gamma M$. In Figure 6.4(a) and Figure 6.4(b) the light is TE polarized, i.e. the electric field is set perpendicular to the plane of reflection. In Figure 6.4(c) and Figure 6.4(d) the light is TM polarized, i.e. the electric field is set parallel to the plane of reflection. The reflectivity is taken in the wavelength range between $1.1\mu m$ to $1.9\mu m$ in steps of $10nm$, displayed on the horizontal axis. After dividing out the spectrum of the light incident to the sample, recorded at the position of the sample, the curves represent the absolute reflectivity. The curves are vertically shifted for a better visualization of spectrally shifting peaks with the angle of incidence. Measurements where performed for angles from $\vartheta = 10°$ to $\vartheta = 70°$ in steps of $5°$ as displayed from bottom to top in Fig. 6.4.

A comparison of the four graphs in Figure 6.4 shows that there is a clear difference in spectra for the different symmetry directions and polarizations. The curves in the
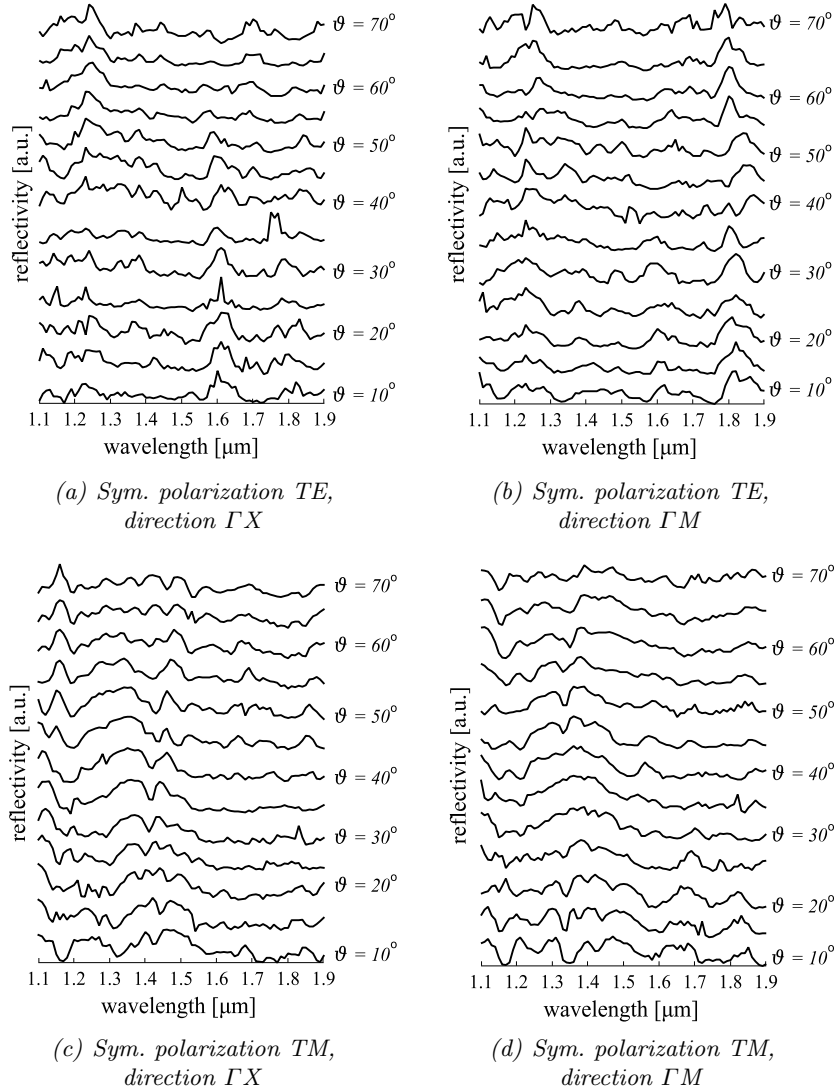
*(a) Sym. polarization TE,
direction ΓX*

*(b) Sym. polarization TE,
direction ΓM*

*(c) Sym. polarization TM,
direction ΓX*

*(d) Sym. polarization TM,
direction ΓM*

**Figure 6.4:** *Experimental reflectivity data of the PhC for the symmetry directions ΓX and ΓM and TE and TM polarization. The curves are vertical shifted for clarity, from bottom to top, the angle of incidence increases from $\vartheta = 10°$ to $\vartheta = 70°$.*

four graphs also show that at these wavelengths the spectra contain many resonances of different shapes with a weak $\vartheta$ dependence. The next section gives a closer analysis of the individual resonances in the spectra. To retrieve from the observed spectral features, independent of their asymmetry, the center frequency ($\omega_0$) and bandwidth ($\gamma$).

## 6.4   Experimentally Extracted Q-factors

A closer investigation reveals that the resonances possess different line shapes, such as maxima, minima, and dispersive (asymmetric) forms. In Section 2.7 the origin of dispersive line shapes has been explained as interference between light directly (Fresnel) reflected at

the PhC surface and part of the light that first couples to the PhC leaky modes, and thus experiences a phase shift. The center frequency ($\omega_0$) and width ($\gamma$) of these resonances are direct related with the leaky modes' quality factor via Eq. 2.8. Fano functions (Eq. 2.12) are fitted to non overlapping resonances. Two additional fit parameters are required for such fits, an offset and a scaling factor, which, however, supposed to leave the retrieved center frequency, line width unchanged.

Figure 6.5 shows an example of three Fano fits to demonstrate its suitability to describe the resonances found in the reflectivity curves of Fig. 6.4. All of the graphs contain a selection of the experimental data in which an individual resonance can be identified that hardly shows any overlap with neighbour resonances. Besides the fitted curves, also the fit parameters obtained are displayed in the graphs from which the leaky mode quality factor is calculated. During the fit, $q$ is restricted to values between -1 and +1 (compare to Fig. 2.9).
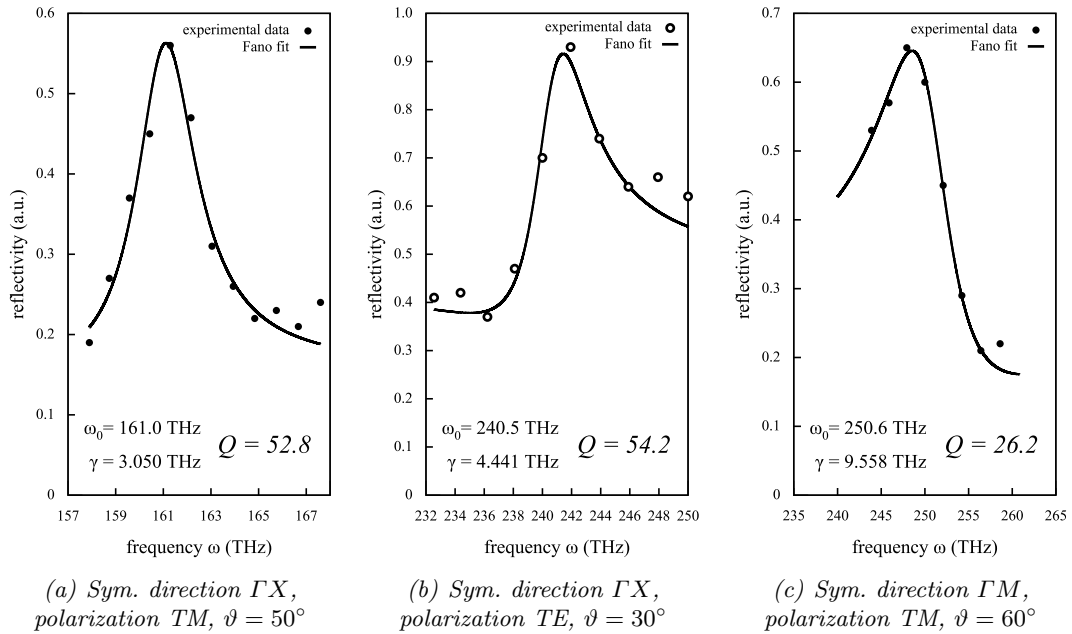


(a) Sym. direction $\Gamma X$, polarization TM, $\vartheta = 50°$

(b) Sym. direction $\Gamma X$, polarization TE, $\vartheta = 30°$

(c) Sym. direction $\Gamma M$, polarization TM, $\vartheta = 60°$

**Figure 6.5:** *Example of three Fano fits to determine the resonance center frequency and linewidth and calculate the leaky mode's quality factor from that. The resonance in (a) has a Q-factor of 52.8, in (b) the Q-factor is 54.2 and in (c) a factor of 26.2.*

The quality factor is calculated for a total of 225 resonances found in the experimental reflection data with normalized center frequencies between 0.5–0.9 (wavelength range 1.1–1.9 $\mu m$). In this frequency range higher order modes lie above the designed band gap.

Using the center frequencies obtained by the fits, in Figure 6.6 the dispersion curves of the identified leaky modes are constructed in a banddiagram. The center frequencies $\omega_0$ obtained from the Fano fits in combination with the symmetry direction and the incident angle $\vartheta$ limits the dots inside the banddiagram to a single position. Dots that belong

to the same mode are connected with a black line. Within the figure we have chosen
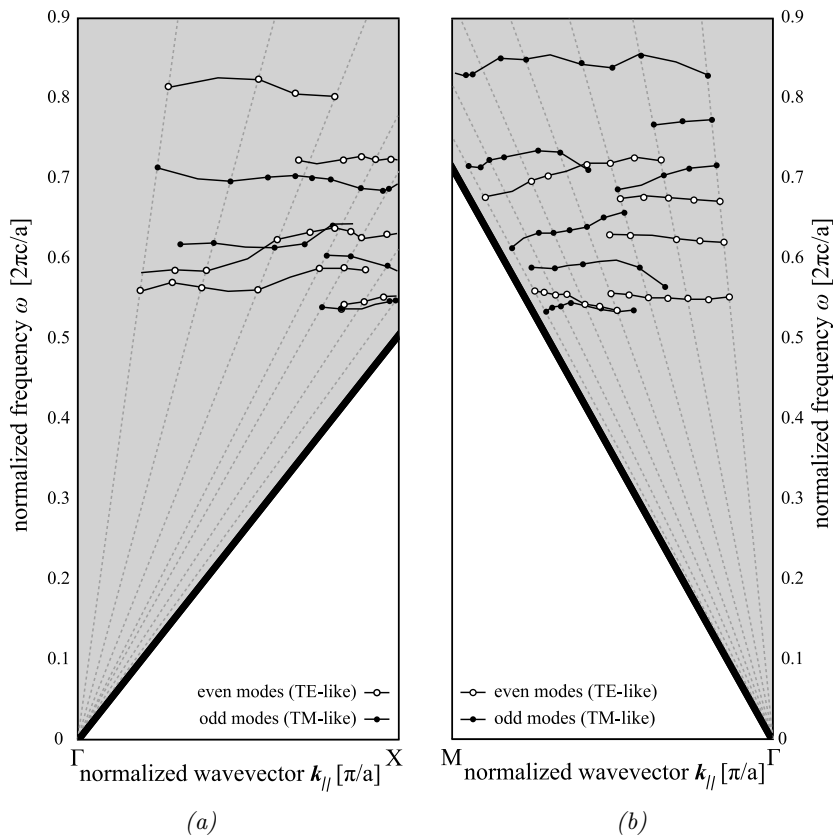


**Figure 6.6:** Reconstruction of the leaky modes in a banddiagram.

to add only the measured dispersion curves and not to add any theoretical dispersion curves. Although it would be possible to fit simulations to the measured curves, we found it inconvenient due to the high mode density in the measured frequency range.

The distribution of calculated quality factors are displayed in the histograms of Figure 6.7. The histograms 6.7(a,b,d,e) contain the quality factor distribution for the polarizations and the individual symmetry directions. The histograms 6.7(c,f) only makes a difference in the two polarization states, the symmetry directions are discarded. The histograms show that quality factors have values that vary from 17 to 140 for TE modes, and values of 23 to 1500 for TM modes.

## 6.5 Results and Comparison with Theory

When comparing the calculated intrinsic quality factors (Fig. 5.3) with the measured quality factors (Fig. 6.7), one notices that the intrinsic quality factors have values from 60 to 1800 and that the measured quality factors have values from 17 to 140, and thus are in general lower. This discrepancy between theory and experiment can have two possible
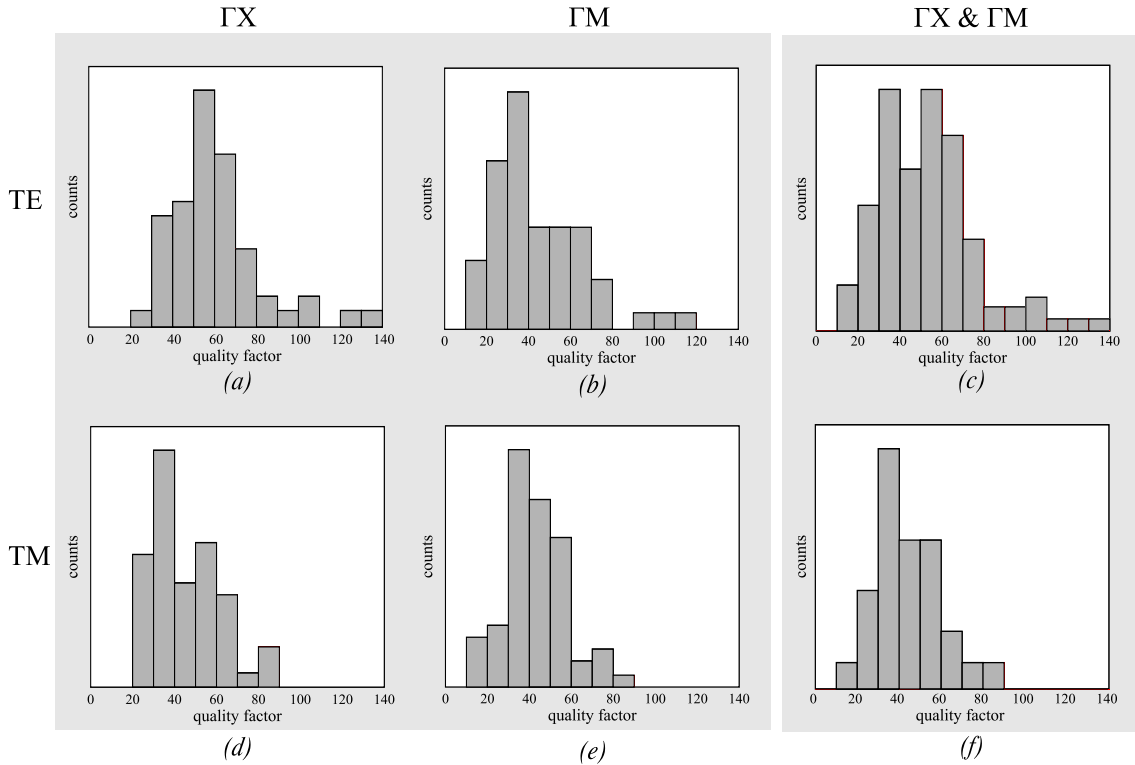
**Figure 6.7:** *Quality factor histograms: (a) TE, ΓX; (b) TE, ΓM; (c) TE; (d) TM, ΓX; (e) TM, ΓM and (f) TM.*

explanations. First, if the spectral resolution of our set-up would habe been to low, it would have limited the contrast of the resonances, which results in broad resonances with low quality factors. In our set-up, however, the spectral resolution is limited by the monochromator to $3.5nm$, which gives an estimated quality factor restriction up to $Q = 300$. Since we have never found quality factors of 300 in our reflection spectra, we know that this first explanation can not explaining the discrepancy. Second, as described in Chapter 2.5, we explain the discrepancy to fabrication imperfections which introduces extra (extrinsic) losses.

In order to improve the quality factor, it is advised to search for the most dominant loss factor. For this I recommend extra quality factor studies (simulations) on samples, incorporating one loss mechanism at a time. As LIL provides an excellent periodicity over a large area, I do not expect that hole displacements has a significant influence on the quality factors in our sample. Loss mechanisms from which I expect to have a significant influence on the mode quality factors are any cracks from hole to hole and any roughness inside and on the walls of the holes.

In the next chapter the results of the transmission experiment and the reflection experiments are summarized.

# Chapter 7

# Conclusions

We have carried out a linear reflection and transmission experiment on a 2D PhC slab in the NIR. By comparison to several theoretical models, additional information is gained on the fabrication quality as can be obtained with a novel type of laser interference lithography for fabricating large area, high contrast 2D Silicon PhC's. The described optical characterization also form the basis for subsequent investigation of third-order nonlinear effects in a 2D PhC slabs, where two-photon absorption is suppressed.

To our knowledge the presented transmission spectra are the first ones obtained from a LIL fabricated 2D PhC slab supported by a waver substrate. Within the transmission spectra we find sharp resonances superimposed on a Fabry-Pérot fringes background. These sharp resonances are the result of interferences between direct transmitted light and light that first coupled to the PhC leaky modes and diffract out with a certain phase delay. The Fabry-Pérot fringes are formed due to reflections from the planar transparent layers the PhC consist of.

The measured transmission spectra are compared to a theoretical model to obtain the structural parameters for our sample. Based on these structure parameters the theoretical upper limit for the quality factors (intrinsic losses) are predicted for the PhC leaky modes.

In reflection the PhC is investigated for NIR wavelengths. Within the reflection spectra Fano-like resonances appear as well, due to coupling of external radiation to the PhC leaky modes. The shape and spectral position of individual resonances are fitted by a Fano-function to determine the resonance center frequency and the total $Q$-factors, which also includes extrinsic losses.

The measured quality factors are compared to the theoretically calculated quality factors showing that the latter are about 8 times higher. The discrepancies are due to unwanted fabrication imperfections. Those imperfections are the so-called extrinsic losses, such as cracks and roughnesses inside and on the walls of the holes, or the polydispersity

of the hole diameters.

In summary the data presented here are the first measurements of quality for large area high index PhC slabs. The obtained values for the $Q$-factors of individual modes should be of high importance for a realistic judgement of resonant field enhancements in subsequent investigations on optically nonlinear switching effects.

# Acknowledgements

To all good things comes an end, so does the period in which I was called a student. During this period I met some nice people which I have to express my deepest appreciation to.

First, I'd like to thank Klaus Boller for the incredible learning experience he offered me in his group as well for the suggestions for improving this thesis. Petra Groß, Liviu Prodan and Roel Arts, the good help, guidance and suggestions I received on a daily basis where always very neat. I couldn't wish myself a better team for this project. Good luck with the rest of your lives and careers. I'd like to thank Kobus Kuipers for his suggestions and answers about the experiments which made sure I was heading into the right direction. Alfred Schirmacher, thanks for the opportunity you gave us to measure the transmission of the sample at PTB, all your preparations and help made it a very efficient time. For the succeeding of my project I also have to give a major thanks to Peter van der Slot. His advice on one of the last simulations I performed where key for my project. Thanks to Hugo Hoekstra to complete my graduation committee.

Traveling an hour by train to my office at the Laser Physics and Nonlinear Optics group wasn't a commitment at all. The people of the group made it always a pleasant arrival for me. The different trips, parties and moments of relaxation by playing cards during lunch made it a period I shall not soon forget. Especially the times I made you all loose. Merel, sorry for the bad competition I gave you with websudoku.

The friends I gained from my HTS period are also not to forget. I enjoyed the time we spend together in and out of school and the vacations we had. Extra thanks to those who always offered me a bed on the ground after a night of going out.

My parents and sisters are the one who I give the most credits. There support and encouragements made that I never lost focus to get the best out of myself. Also friends and family who showed there interest in me,...thanks.

Yours,

*Ronald Hagen*

Enschede, September 2007

# Bibliography

[1] V. Astratov, I. Culshaw, R. Stevenson, D. Whittaker, M. Skolnick, T. Krauss, and R. de La Rue, "Resonant coupling of near-infrared radiation to photonic band structure waveguides," *Journal of Lightwave Technology*, vol. 17, pp. 2050–+, Nov. 1999.

[2] C. Grillet, D. Freeman, B. Luther-Davies, S. Madden, R. McPhedran, D. Moss, M. Steel, and B. Eggleton, "Characterization and modeling of Fano resonances in chalcogenide photonic crystal membranes," *Optics Express*, vol. 14, pp. 369–+, Jan. 2006.

[3] D. Coquillat, A. Ribayrol, R. de La Rue, M. Le Vassor D'Yerville, D. Cassagne, and C. Jouanin, "First Observations of 2D Photonic Crystal Band Structure in GaN-Sapphire Epitaxial Material," *Physica Status Solidi Applied Research*, vol. 183, pp. 135–138, Feb. 2001.

[4] V. Pacradouni, W. Mandeville, A. Cowan, P. Paddon, J. F. Young, and S. R. Johnson, "Photonic band structure of dielectric membranes periodically textured in two dimensions," *Phys. Rev. B*, vol. 62, pp. 4204–4207, Aug 2000.

[5] A. Cowan, P. Paddon, V. Pacradouni, and J. Young, "Resonant scattering and mode coupling in two-dimensional textured planar waveguides," *J. Opt. Soc. Am. A*, vol. 18, pp. 1160–1170, 2001.

[6] M. Netti, A. Harris, J. Baumberg, D. Whittaker, M. Charlton, M. Zoorob, and G. Parker, "Optical trirefringence in photonic crystal waveguides," *Phys. Rev. Lett.*, vol. 86, pp. 1526–1529, Feb 2001.

[7] M. Galli, M. Agio, L. Andreani, L. Atzeni, D. Bajoni, G. Guizzetti, L. Businaro, E. D. Fabrizio, F. Romanato, and A. Passaseo, "Optical properties and photonic bands of gaas photonic crystal waveguides with tilted square lattice," *The European Physical Journal B - Condensed Matter and Complex Systems*, vol. 27, no. 1, pp. 79–87, 2002.

[8] K. Crozier, V. Lousse, O. Kilic, S. Kim, S. Fan, and O. Solgaard, "Air-bridged photonic crystal slabs at visible and near-infrared wavelengths," *Phys. Rev. B*, vol. 73, no. 11, p. 115126, 2006.

[9] J. Joannopoulos, R. Meade, and J. Winn, *Photonic Crystals : Molding the Flow of Light*. Princeton: Princeton University press, 1995.

[10] H. Ibach and H. Lüth, *Solid-State Physics : An Introduction to Principles of Materials Science*. Springer, 2nd ed., 1995.

[11] T. Ochiai and K. Sakoda, "Nearly free-photon approximation for two-dimensional photonic crystal slabs," *Phys. Rev. B*, vol. 64, p. 045108, Jul 2001.

[12] S. G. Johnson, S. Fan, P. R. Villeneuve, J. Joannopoulos, and L. Kolodziejski, "Guided modes in photonic crystal slabs," *Phys. Rev. B*, vol. 60, pp. 5751–5758, Aug 1999.

[13] E. Flück, *Local interaction of light with periodic photonic structures*. PhD thesis, Optical Techniques Group (OT), Department of Science and Technology, University of Twente, 2003.

[14] P. Villeneuve, S. Fan, S. Johnson, and J. Joannopoulos, "Three-dimensional photon confinement in photonic crystals of low-dimensional periodicity," *IEE Proceedings - Optoelectronics*, vol. 145, no. 6, pp. 384–390, 1998.

[15] O. Painter, J. Vučković, and A. Scherer, "Defect modes of a two-dimensional photonic crystal in an optically thin dielectric slab," *Journal of the Optical Society of America B Optical Physics*, vol. 16, pp. 275–285, Feb. 1999.

[16] W. Bogaerts, P. Bienstman, D. Taillaert, R. Baets, and D. de Zutter, "Out-of-plane scattering in 1-D photonic crystal slabs," *Optical and Quantum Electronics*, vol. 34, pp. 928–934, 2002.

[17] S. Fan and J. D. Joannopoulos, "Analysis of guided resonances in photonic crystal slabs," *Phys. Rev. B*, vol. 65, p. 235112, Jun 2002.

[18] S. Johnson. Meep Introduction: `http://ab-initio.mit.edu/wiki/index.php/Meep_Introduction`.

[19] C. Bostan, *Design and Fabrication of quasi-2D Photonic Crystal Components based on Silicon–on–Insulator Technology*. PhD thesis, Integrated Optical Microsystems (IOMS), Faculty of Electrical Engineering, Mathematics and Computer Science, University of Twente, 2005.

[20] W. Bogaerts, P. Bienstman, and R. Baets, "Scattering at sidewall roughness in photonic crystal slabs," *Optics Letters*, vol. 28, pp. 689–691, May 2003.

[21] Y. Tanaka, T. Asano, Y. Akahane, B.-S. Song, and S. Noda, "Theoretical investigation of a two-dimensional photonic crystal slab with truncated cone air holes," *Applied Physics Letters*, vol. 82, no. 11, pp. 1661–1663, 2003.

[22] S. Hughes, L. Ramunno, J. F. Young, and J. E. Sipe, "Extrinsic optical scattering loss in photonic crystal waveguides: Role of fabrication disorder and photon group velocity," *Physical Review Letters*, vol. 94, no. 3, p. 033903, 2005.

[23] *Diffraction of Water Waves.* website: `http://www.ngsir.netfirms.com/englishhtm/Diffraction.htm`.

[24] U. Fano, "Effects of configuration interaction on intensities and phase shifts," *Phys. Rev.*, vol. 124, pp. 1866–1878, Dec 1961.

[25] *Manual DiffractMOD v1.0.* website: `http://www.rsoftdesign.com/`.

[26] J.-P. Berenger, "A perfectly matched layer for the absorption of electromagnetic waves," *Journal of Computational Physics*, vol. 114, pp. 185–200, Oct. 1994.

[27] E. Popov, M. Nevière, B. Gralak, and G. Tayeb, "Staircase approximation validity for arbitrary-shaped gratings," *J. Opt. Soc. Am. A*, vol. 19, pp. 33–42, 2002.

[28] S. Johnson and J. Joannopoulos, "Block-iterative frequency-domain methods for maxwell's equations in a planewave basis," *Opt. Express*, vol. 8, pp. 173–190, Jan. 2001.

[29] S. Johnson. MPB Introduction: `http://ab-initio.mit.edu/wiki/index.php/MPB_Introduction`.

[30] M. Cryan, M. Hill, D. Sanz, P. Ivanov, P. Heard, L. Tian, S. Yu, and J. Rorison, "Focused ion beam-based fabrication of nanostructured photonic devices," *IEEE Journal of Selected Topics in Quantum Electronics*, vol. 11, pp. 1266–1277, Nov.-Dec. 2005.

[31] T. Krauss, Y. Song, S. Thoms, C. Wilkinson, and R. de la Rue, "Fabrication of 2-d photonic bandgap structures in gaas/algaas," *Electronics Letters*, vol. 30, no. 17, pp. 1444–1446, 1994.

[32] Y. Vladimirsky, A. Bourdillon, O. Vladimirsky, W. Jiang, and Q. Leonard, "Demagnification in proximity x-ray lithography and extensibility to 25 nm by optimizing fresnel diffraction," *Journal of Physics D: Applied Physics*, vol. 32, no. 22, pp. L114–L118, 1999.

[33] W. Bogaerts, V. Wiaux, D. Taillaert, S. Beckx, B. Luyssaert, P. Bienstman, and R. Baets, "Basic structures for photonic integrated circuits in silicon-on-insulator," *Optics Express*, vol. 12, no. 8, pp. 1583–1591, 2002.

[34] L. Vogelaar, W. Nijdam, H. van Wolferen, R. de Ridder, F. Segerink, E. Flck, L. Kuipers, and N. van Hulst, "Large area photonic crystal slabs for visible light with waveguiding defect structures: Fabrication with focused ion beam assisted laser interference lithography," *Adv. Mater.*, vol. 13, no. 20, pp. 1551–1554, 2002.

[35] L. Prodan, T. Euser, H. Wolferen, C. Bostan, R. Ridder, R. Beigang, K.-J. Boller, and L. Kuipers, "Large-area two-dimensional silicon photonic crystals for infrared light fabricated with laser interference lithography," *Nanotechnology*, vol. 15, no. 5, pp. 639–642, 2004.

[36] Soitec. Parc Technologique des Fontaines, 38190 Bernin, France. website: `http://www.soitec.com`.

[37] V. Lousse, W. Suh, O. Kilic, O. Solgaard, and S. Fan, "Angular and polarization properties of a photonic crystal slab mirror," *Optics Express*, vol. 12, no. 8, 19 April 2004.

[38] V. Astratov, M. Skolnick, S. Brand, T. Krauss, O. Karimov, R. Stevenson, D. Whittaker, I. Culshaw, and R. de La Rue, "Experimental technique to determine the band structure of two-dimensional photonic lattices," *IEE Proc., Optoelectron.*, vol. 145, pp. 398–402, Dec 1998.

# Appendix A:
# Two-color Characterization of a 2D Photonic Crystal

Poster presented at FOM-meeting Physics @ Veldhoven 2007, 23–24 January 2007.

# Two-color characterization of a 2D photonic crystal

R. Hagen,[a] R. Arts,[a] L. Prodan,[a] P. Gross,[a] L. Kuipers[b,c] and K-J Boller[a]

a. Laser Physics and nonlinear Optics group, Department of Science & Technology, University of Twente
b. Optical Techniques Group, Department of Science & Technology, and MESA+ Research Institute, University of Twente
c. Center for Nanophotonics, FOM-Institute for Atomic and Molecular Physics (AMOLF)
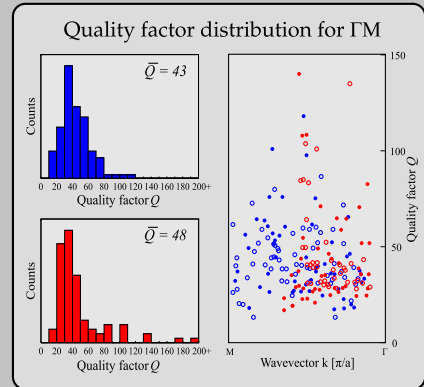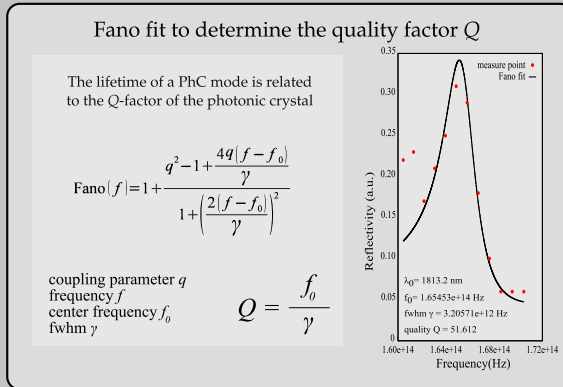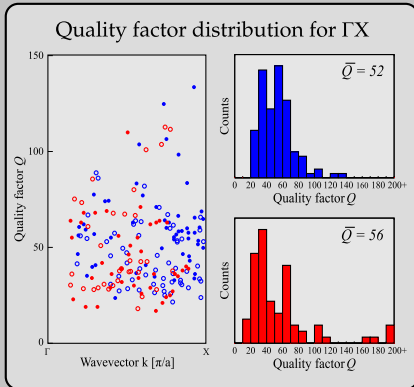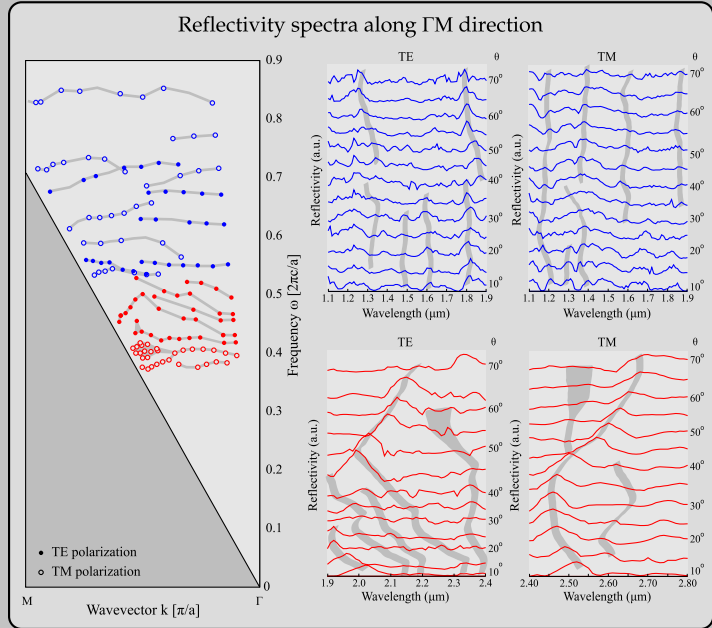
**FOM**

**University of Twente**
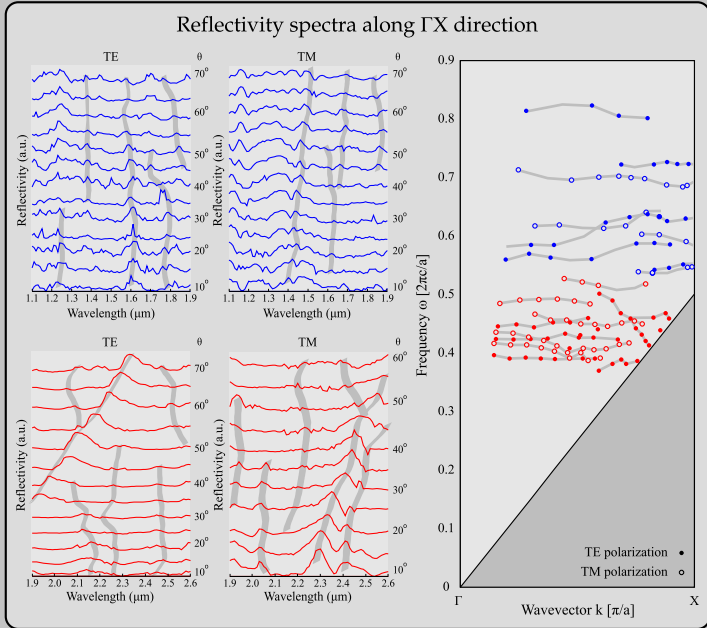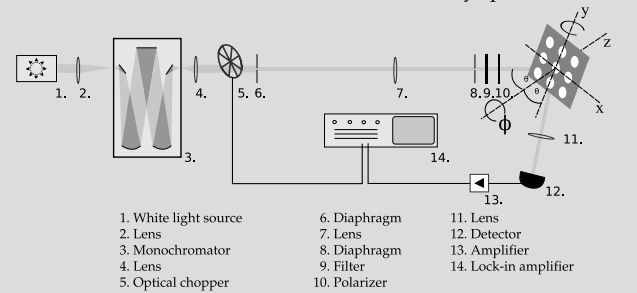**Enschede - The Netherlands**

**Goal of the Project:** As preparation for studies of the nonlinear properties of a photonic crystal (PhC), we have carried out a linear reflectivity characterization in the MIR range around 2.5 μm and, also, in the range of half of those wavelengths (around 1.25 μm). The latter, and comparison with the theoretically expected band structure, should provide additional information on the optical properties of the fabricated crystals.

**Photonic Crystal:** Schematic drawing of a 2D PhC. The sample is fabricated with Laser Interference Lithography (LIL) to create a large area crystal[1].



First Brillouin zone in reciprocal space
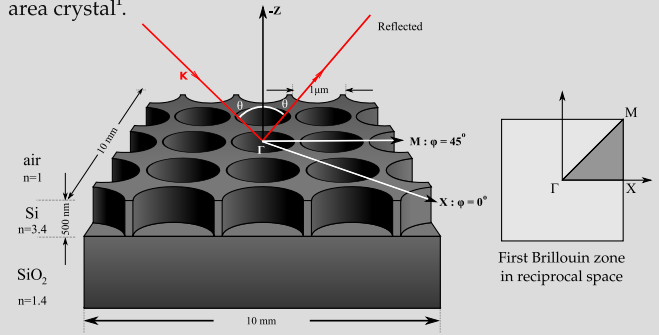
**Method of Investigation[2]:** Measure the reflectivity as a function of wavelength along the two symmetry directions ΓX and ΓM for a range of incident angles θ. Information on the mode structure can be obtained from Fano-like features[3] in the reflectivity spectra.



1. White light source
2. Lens
3. Monochromator
4. Lens
5. Optical chopper
6. Diaphragm
7. Lens
8. Diaphragm
9. Filter
10. Polarizer
11. Lens
12. Detector
13. Amplifier
14. Lock-in amplifier

## Reflectivity spectra along ΓX direction



## Reflectivity spectra along ΓM direction



TE polarization ·
TM polarization ○

## Quality factor distribution for ΓX



$\overline{Q} = 52$

$\overline{Q} = 56$

## Fano fit to determine the quality factor Q

The lifetime of a PhC mode is related to the Q-factor of the photonic crystal

$$\text{Fano}(f) = 1 + \frac{q^2 - 1 + \frac{4q(f - f_0)}{\gamma}}{1 + \left(\frac{2(f - f_0)}{\gamma}\right)^2}$$

coupling parameter $q$
frequency $f$
center frequency $f_0$
fwhm $\gamma$

$$Q = \frac{f_0}{\gamma}$$



$\lambda_0$ = 1813.2 nm
$f_0$ = 1.65453e+14 Hz
fwhm $\gamma$ = 3.20571e+12 Hz
quality Q = 51.612

measure point ·
Fano fit —

## Quality factor distribution for ΓM



$\overline{Q} = 43$

$\overline{Q} = 48$

## Conclusions

The Q-factor for a 2D photonic crystal is determined from resonance features in reflectivity spectra measured with two colors.

The experiments yield an average Q-factor of 50 with a deviation of 29.

### References

[1] L. Prodan, T.G. Euser, H.A.G.M. van Wolferen, C. Bostan, R.M. de Ridder, R. Beigang, K-J Boller and L. Kuipers, Nanotechnology 15, 639 (2004)
[2] V. N. Astratov, I. S. Culshaw, R. M. Stevenson, D. M. Whittaker, M. S. Skolnick, T. F. Krauss, and R. M. De La Rue, J. Lightwave Techn. 17, 2050 (1999)
[3] U. Fano, Phys. Rev. 124, 1866 (1961).